

Microstructural and Compositional Control in Chiton Ocelli Lenses

Leanne Friedrich

Northwestern University Materials Science - Senior Honors Thesis

March 16, 2015

Advisor: Derk Joester

Abstract

In a technique seen only in two other organisms, the chiton *Acanthopleura granulata* utilizes mineralized lenses for vision. The chiton is the only organism known to possess polycrystalline, aragonitic lenses, and little is known about the processes by which the lens is formed. With Electron Backscatter Diffraction (EBSD), Energy Dispersive Spectroscopy (EDS), and etching, this study elucidates the interplay between lens nucleation and growth and the microstructure of the lens. In the presence of organic materials, the lens nucleates a polycrystalline, twinned core. The entire lens grows from the single core, producing large, twinned grains with a fan-like morphology and consistent $\langle 001 \rangle$ axis orientation. Through transmission of light and images and simulations, this study demonstrates the unique imaging qualities of the lenses. Birefringence and polycrystallinity coupled with the skewed aragonitic $\langle 001 \rangle$ axis produce double images and large longitudinal aberrations, decreasing image quality without eliminating the potential for spatial imaging.

Contents

1	Introduction.....	1
1.1	Motive.....	1
1.2	Structure of Ocelli.....	1
1.3	Role of microstructure in optical properties.....	2
1.4	Role of impurities in optics.....	3
2	Methods.....	4
2.1	Sample Preparation.....	4
2.2	Electron Backscatter Diffraction (EBSD).....	4
2.3	Detection of Impurities.....	6
2.4	X-ray microtomography.....	6
2.5	Simulations.....	6
2.6	Transmitting Light.....	8
2.6.1	Polarized Light.....	8
2.6.2	Image Transmission.....	8
2.6.3	Ray Transmission.....	9
3	Formation of the Lens.....	10
3.1	Microstructure.....	10
3.1.1	Lens, shell, and cornea are composed of polycrystalline aragonite.....	10
3.1.2	Grains are aligned in lens, cornea, and shell.....	13
3.1.3	Twinning is prevalent in the lens.....	16
3.2	Impurities.....	19
3.2.1	The lens-shell interface contains organic matter.....	19
3.2.2	Bands demonstrate the direction of growth.....	21
3.2.3	Pores at the lens-shell interface indicate a potential nucleation point.....	24
3.2.4	Regional compositional differences demonstrate impurity localization.....	24
3.3	X-ray microtomography.....	27
3.4	Discussion.....	29
4	Performance of the Lens.....	30
4.1	Simulations.....	30
4.1.1	Total internal reflection and aberrations vary between air and water.....	30
4.1.2	(001) axis orientation impacts focal length and longitudinal aberration.....	30
4.1.3	(001) axis orientation impacts transverse aberration.....	31

4.1.4	$\langle 001 \rangle$ axis orientation impacts horizontal displacement	32
4.1.5	Aberrations result from crystallographic asymmetry	32
4.1.6	Incident ray orientation impacts focal length and aberrations	32
4.1.7	Grain Boundary Orientation Impacts Transmission	32
4.2	Transmission	35
4.2.1	Polarized light reveals crystallography	35
4.2.2	The lens transmits images	35
4.2.3	Laser ray tracing demonstrates aberrations in the lens	37
4.3	Discussion	41
5	Conclusions	42
6	References	43
7	Acknowledgments	45

1 Introduction

1.1 Motive

Biom mineralization, or the processes by which organisms form mineralized structures, enlighten basic science and inspire new material fabrication processes and structures. The study of biominerals has informed medical advances, particularly in tooth and bone health. Biominerals like nacre and sponge spicules have inspired materials with advanced mechanical properties.^[1-5] Research into the formation of calcium carbonate polymorphs shows promise for carbon capture, and fabrication processes inspired by biomineral growth can reduce industrial emissions and waste.^[6-8] Biominerals may inspire the sustainable production of advanced materials.

Chitons, a diverse class of tidal mollusks, produce several biominerals, including hard magnetite teeth^[9] and aragonitic spines and shells (Figure 1A). These structures can inspire the production of dopant-hardened ceramics^[9] and two-dimensional photonic crystals. An additional, less studied, structure known as the chiton ocellus may improve the fabrication of aragonite crystals with intricately designed microstructure and self-assembly of curved microlens arrays.

Ocelli are sensory structures embedded in the aragonitic shells of some chiton species (Figure 1B). Initial studies indicate that ocelli may allow chitons to visualize their surroundings. Compared to the eyeless chiton *Chaetopleura apiculata*, the chiton *Acanthopleura granulata* responds more to objects than decreases in illumination, suggesting that ocelli support spatial imaging.^[10] Ocelli uniquely possess mineralized lenses. Only two other organisms are known to possess mineralized lenses. Trilobites, extinct marine animals, have compound eyes containing calcitic lenslets which extinguish birefringence through microstructure and orientation control.^[11-18] Brittlestars use single-crystalline calcite lenses to focus light with minimal aberration onto single sensory spots, allowing them to respond to changes in illumination.^[19, 20] Lessons learned from brittlestars and trilobites have inspired research in ceramic microlens arrays. Self-assembled calcium carbonate microlens arrays demonstrate promise for their high refractive indices and sustainable fabrication processes.^[21-23] However, their polycrystallinity may interfere with optical quality. Because ocelli are also polycrystalline, they may hold the key to controlling the crystallographic orientation of synthetic microlens arrays, thereby improving their optical quality.

This study of chiton ocelli aims to answer two outstanding questions. First, what do chitons see? Do chiton ocelli exhibit advanced optical properties, and what advantages do ocelli offer to chitons? Second, how are ocelli formed? In previous studies, no partially formed ocelli were found, and little is known about the nucleation and growth of the structures. The formation processes behind chiton ocelli can inspire the bottom-up fabrication of crystallized microlenses.

1.2 Structure of Ocelli

Ocelli are composed of an aragonitic lens and cornea suspended above a cell cavity known as the rhabdom (Figure 1C,D). The rhabdom is surrounded by a retina, which is surrounded by pigmented aragonite. Sensory cells run from the retina, through aesthetes, which are sensory and secretory channels prevalent throughout the shell, towards pallial nerve cords below the dorsal epithelium^[24].

The rhabdom is characterized by a continuous array of $0.1\ \mu\text{m}$ by $7\ \mu\text{m}$ microvilli rooted in the retina. The microvilli run parallel to the surface of the shell and are radially arranged around a central axis, though they are less organized at the base of the rhabdom. Each retina contains roughly 100-170 axons which are $5\text{-}8\ \mu\text{m}$ wide.^[10,24]

The lens, cornea and shell are all composed of aragonite^[10]. In *A. granulata*, lenses range in width from $50\text{-}60\ \mu\text{m}$, with many lenses exhibiting oval cross-sections.^[25]

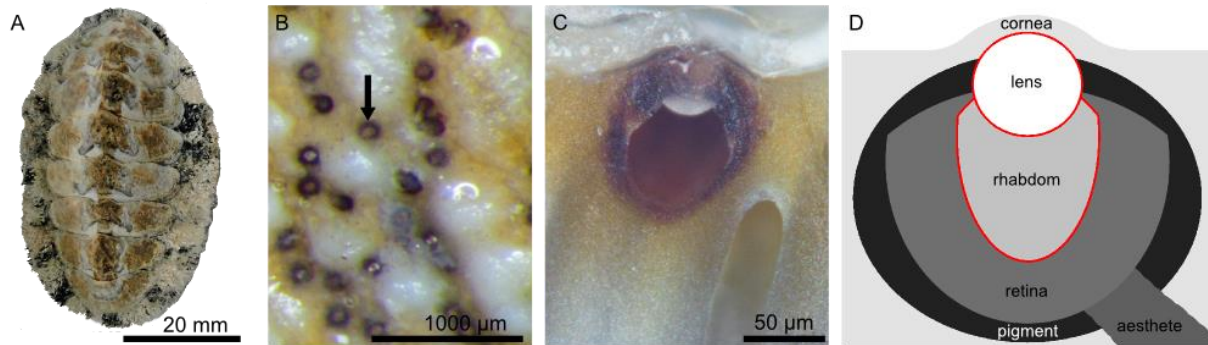


Figure 1. Morphology of *Acanthopleura granulata* and ocelli. A) *A. granulata*. B) *A. granulata* valve. Arrow points to one of many ocelli. C) Cross-section of ocellus. Lens is partially obscured by pigmented shell. D) Diagram of ocellus.

1.3 Role of microstructure in optical properties

While aragonite lends a high refractive index to ocelli lenses, thereby decreasing their focal length, the material's birefringence presents a potential issue for the lens. Aragonite is biaxial and birefringent, containing three distinct refractive indices ($n_\alpha = 1.530$, $n_\beta = 1.680$, $n_\gamma = 1.686$).^[26] Because the material is birefringent, the refractive index of aragonite depends on the orientation of the light passing through it. In an amorphous material, light passes through the entire material in one continuous path (Figure 2A). In a birefringent material, if the entire crystal has the same lattice orientation (i.e. it is a single crystal), light passes through the entire crystal in two distinct paths (Figure 2B). However, if the crystal contains grains with different orientations, the refractive indices of the two grains will be different for nearly every ray orientation. Therefore, the light path will be diverted within the crystal at grain boundaries (Figure 2C). With few exceptions, grain boundaries cause light to scatter and blur images. Knowing the locations and orientations of grain boundaries is essential for understanding the path of light through a birefringent crystal.

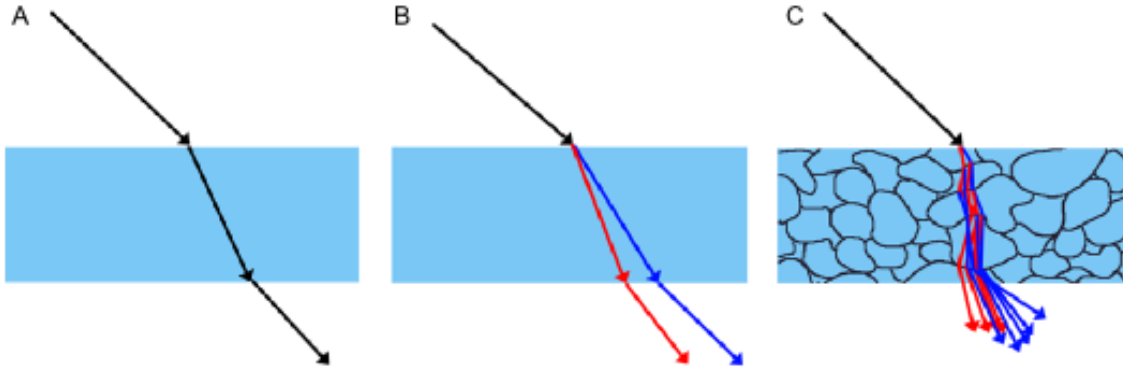


Figure 2. Passage of light through materials. Red and blue rays indicate rays in different eigenstates. A) Isotropic material. B) Birefringent single crystal. C) Birefringent polycrystalline material.

1.4 Role of impurities in optics

Organic and inorganic impurities including proteins, polysaccharides, and ions like magnesium are known to facilitate the nucleation and growth of biominerals, providing control over shape and microstructure.^[27–31] By adsorbing onto select crystallographic planes, impurities could support the formation of curved ocelli. Additionally, some macromolecules have been shown to function as nucleation points which support the growth of single crystalline aragonite and calcite.^[32,33] Proteins in chiton shells may create a single nucleation point for the lens, supporting the growth of a lens with few grains.

All lenses with spherical rather than quadratic curvature exhibit aberrations wherein path differences between the inner and outer portions of the lens induce differing focal lengths for different regions of the lens. This phenomenon, known as spherical aberration, impacts amorphous as well as crystalline lenses. Thicker lenses experience greater spherical aberration, and trilobites and chitons both possess nearly spherical lenses, making them highly susceptible to aberration. Incorporation of organic matter or other low-refractive index materials may correct spherical aberration in ocelli lenses, leading to higher image signal and lower distortion.

In trilobites, a high-magnesium core and bowl limit the spherical aberration of the highly spherical lenslets by incorporating a low-refractive index material into the center and bottom of the lens.^[11,16] Proteins in brittlestar lenses may, likewise, correct spherical aberration, increasing the intensity of light which reaches the sensory cells.^[19] Identification of organic matter in chiton ocelli can explain how the lens could overcome spherical aberration despite its highly spherical shape.

2 Methods

2.1 Sample Preparation

For Electron Backscatter Diffraction and X-ray microtomography, dried *Acanthopleura granulata* specimens collected in the Florida Keys were purchased commercially. For etching and impurity characterization, dried *Acanthopleura granulata* specimens collected in Venezuela were obtained from the University of Alabama. Valves were removed from specimens using tweezers.

Cross-sections were obtained from fractured valve segments and from ocelli which were extracted from shells using a razor blade and placed on a plane of tape. Samples were embedded in epoxy (Epo-Tek 301) and polymerized overnight at room temperature. Cross-sections were exposed using a grinding sequence of 600, 800, and 1200 SiC grit paper and then sequentially polished with 3 μm and 1 μm polycrystalline aqueous diamond suspensions and 0.05 μm alumina suspension. Polished blocks were secured to aluminum scanning electron microscope (SEM) stubs with cyanoacrylate adhesive.

Etched samples were submerged in Millipore water (pH=5.5) and agitated on a rocking table at 30 rpm for 15 minutes. Some samples were coated with 10 nm of Platinum using a Denton Desk III sputter coater and grounded using colloidal silver paint.

For image transmission experiments, a border of nail polish was drawn on a glass slide as a spacer. Ocelli were extracted from shells using a razor blade and placed on the glass slide inside the nail polish border. A cover slip was adhered to the slide on top of the spacer and fully sealed using nail polish.

As a reference sample, portions of a geological aragonite crystal were embedded in epoxy and polished using the previously described grinding and polishing sequence.

Amorphous calcium carbonate (ACC) microlens arrays were prepared according to Lee (2012).^[23] 1 g of CaOH was added to 100 mL of Millipore water. After three days, 23.4 μL of 0.22M Polysorbate 20 was added to the solution, which was then stirred vigorously. The solution was apportioned into 40 mm petri dishes. After 1 hour, microlens films formed at the surface of the solution. The films were skimmed off of the tops of the dishes onto a cover slip, and residual water was wicked from the side of the cover slip using lint-free paper. Cover slips were dried in air, then placed film-side-down onto glass slides and adhered to the slides using nail polish.

2.2 Electron Backscatter Diffraction (EBSD)

Cross sections of 24 lenses, one shell section, and a section of a geological single crystal of aragonite were examined using EBSD. Seven lens sections were in cross section, i.e. perpendicular to the surface of the shell, fifteen were approximately parallel to the surface of the shell (plan sections), and two were oblique.

Uncoated samples were mounted on a 70° pre-tilted SEM sample holder and observed in a FEI Quanta 600F Environmental Field Emission SEM operated at a partial water vapor pressure of 0.9 Torr, an accelerating voltage of 30 keV, and a working distance of 10 mm. Kikuchi patterns were collected from ground and polished specimens at a step size between 0.3 and 1.1 μm using a Hitachi detector. Patterns were processed into maps of crystal orientation using Oxford HKL software.

The Oxford HKL software package was used to produce grain orientation maps and pole figures. Grain size and misorientation between neighboring grains was determined using a critical misorientation of 1° and orthorhombic (Pmmm) symmetry operators for aragonite.^[34–36] Only grains at least ten pixels in size were considered for subsequent analysis.^[37,38]

Kent Distribution analysis was performed using Wolfram Mathematica 10, in part using code adapted from Leong and Carlile's Spak.^[39] $\langle 100 \rangle$, $\langle 010 \rangle$, $\langle 001 \rangle$, and optic axes ($\langle 0.17, 0, 0.97 \rangle$ and $\langle 0.17, 0, -0.97 \rangle$) orientations were determined using Equation 1, where $(e1, e2, e3)$ are Euler angles. Distributions of $\langle 001 \rangle$ axes were fit to sets of points selected using four methods. Only sets including at least 100 points were fit to Kent distributions. The first method includes all points in the lens. The second method uses the Mathematica ChooseClusters function to refine the set of points in the lens to only include points which are in the tightly aligned cluster of $\langle 001 \rangle$ axes. The third method finds the centroid of all points in the lens, collects all points within 5° of the centroid, re-defines the centroid using the new subset, and recurses until the set converges. The fourth method only selects points which are within the largest grain in the lens using a critical disorientation of 1°.

Equation 1

$$\begin{aligned}
 s1 &= \sin(e1) & s2 &= \sin(e2) & s3 &= \sin(e3) \\
 c1 &= \cos(e1) & c2 &= \cos(e2) & c3 &= \cos(e3) \\
 R &= \begin{bmatrix} c1.c3 - s1.c2.s3 & s1.c3 + c1.c2.s3 & s2.s3 \\ -c1.s3 - s1.c2.c3 & -s1.s3 + c1.c2.c3 & s2.c3 \\ s1.s2 & -c1.s2 & c2 \end{bmatrix} \\
 [x \ y \ z] &= R. [u \ v \ w]
 \end{aligned}$$

Misorientation angles between neighboring grains were calculated using the code described in Equation 2 and Equation 3, where R1 and R2 are rotation matrices shown in Equation 1, and S1 and S2 belong to the set of symmetry operators for the Pmmm system. Misorientation axes were measured using Equation 4, where S1 and S2 are the symmetry operators which result in the smallest misorientation angle.

Equation 2

$$MM = R1.R2^{-1}$$

Equation 3

$$Angle = \min \left(\text{acos} \left(\frac{\text{tr}(S1.MM.S2^{-1}) - 1}{2} \right) \right)$$

Equation 4

$$M = S1.MM.S2^{-1}, \quad Axis = \frac{1}{2 * \csc(Angle)} \begin{bmatrix} M(2,3) - M(3,2) \\ M(3,1) - M(1,3) \\ M(1,2) - M(2,1) \end{bmatrix}$$

2.3 Detection of Impurities

Etched, coated samples were observed in a Hitachi S-3400N-II SEM operated at an accelerating voltage of 20 keV, a probe current of 50 μA and a working distance of 10 mm. Additional coated, etched samples were observed in a Hitachi S4800-II cFEG SEM at an accelerating voltage of 15 keV, a probe current of 10 μA and a working distance of 5 mm.

Energy Dispersive Spectroscopy (EDS) spectra were collected from coated, polished samples in a Hitachi SU8030 with an accelerating voltage of 15 keV, a probe current of 15 mA and a working distance of 15 mm.

2.4 X-ray microtomography

Shell segments containing ocelli were embedded in epoxy and manually ground down to 1 mm x 1 mm x 2 mm blocks using SiC grinding paper. X-ray tomography scans were collected by Dr. Stuart Stock at beamline 2-BM at the Advanced Photon Source, Argonne National Laboratory, with a voxel size of 1.45 μm .

2.5 Simulations

Ray tracing simulations followed the path of non-polarized light across four interfaces: environment-cornea, cornea-lens, lens-rhabdom, and rhabdom-shell. The interfaces were modeled as hemi-spheroids centered on the origin, using the Cartesian equation (Equation 5), where the cornea normal is concurrent with the lab z-axis and the optical axis of the lens. While triaxial ellipsoid lenses have been found,^[25] lenses were modeled as oblate ellipsoids in order to distinguish the effects of crystallography from the effects of lens asymmetry on aberrations.

Equation 5

$$\frac{x^2 + y^2}{a^2} + \frac{z^2}{c^2} = 1$$

The lens dimensions a and c were determined from optical images of embedded cross sections (Table 1, Figure 1).

Table 1. Lens dimensions

Interface	a [μm]	c [μm]
environment-cornea	27.3	25.3
cornea-lens	20.0	18.0
lens-rhabdom	20.0	-18.0
rhabdom-shell	33.0	-73.0

An incident principal ray through the origin, and thus the center of the lens, was generated in the environment above the lens. In some simulations, the incident principle ray was rotated counter-clockwise

around the positive lab y -axis by an angle β (Figure 3). Parallel rays in azimuthal increments of 45° were generated in each of three rings surrounding the principle ray at a distance of $6.7 \mu\text{m}$ (paraxial), $13.3 \mu\text{m}$ (intermediate), and $20 \mu\text{m}$ (peripheral). All rays were modeled as collimated, unpolarized light with a wavelength $\lambda = 500 \text{ nm}$.

For ray tracing, the environment was modeled as air ($n = 1$) or water ($n = 1.33$); the cornea as an isotropic material with the average refractive index of aragonite ($n = 1.632$); the lens as a single crystal of aragonite ($n_\alpha = 1.530$, $n_\beta = 1.680$, $n_\gamma = 1.686$) and the rhabdom as water.

The orientation of the aragonite lattice in the lens was such that the crystallographic axes of the lattice were aligned with the lab axes. In some experiments, the $[001]$ axis was rotated clockwise around the positive $[010]$ direction by an angle α (Figure 3). In some simulations, an interface parallel to the lab (001) plane and through the origin was added, splitting the lens into two grains. In one simulation, these grains were twins, where the upper grain matched the $\alpha = 0^\circ$ orientation, and the lower grain's $[010]$ axis was rotated 64° counterclockwise about the positive $[001]$ axis. A non-twin grain boundary was simulated by rotating the $[001]$ direction of the lower crystal by 64° about the $[010]$ direction.

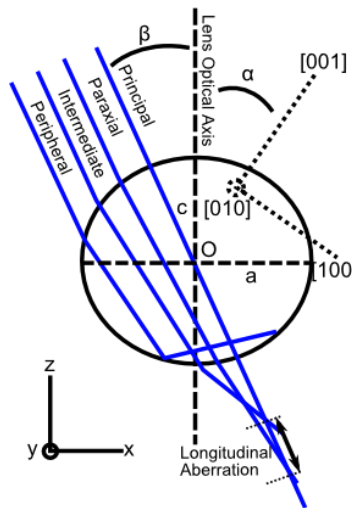


Figure 3. Diagram of ray tracing simulation

Aragonite exhibits biaxial birefringence. Thus, any ray propagating in aragonite has one of two eigenstates, which represent a polarization and refractive index. Here, 'high' and 'low' indicate the eigenstate of rays. Rays passing from an isotropic material into aragonite are each split into a high and a low ray. Rays passing from aragonite into the rhabdom do not split. Depending on the angle of incidence at any given interface, rays may be partially or totally internally reflected. Polaris, a software package designed to model complex optical systems, was used to calculate the deflection of high and low rays across each interface in the model.^[40]

After passing through the lens, paraxial, intermediate and peripheral rays are deflected towards, but do not necessarily intersect the principal ray. Focal points F_i were therefore calculated for each non-principal ray as the point on the principal ray which is closest to the ray in question. Unless otherwise noted, the focal

length f for a given set of rays was calculated as the mean distance of all focal points from the origin. Longitudinal spherical aberration was calculated as the distance δ between the shortest paraxial and the longest peripheral focal length. The position of the ellipse of least confusion for a given set of rays was determined as the distance l_e from the origin at which the mean squared displacement of all rays from the principal ray is minimized. The major and minor axes of the ellipse of least confusion measure the distance between the maximum and minimum x and y dimensions of points on the ellipse of least confusion. Transverse spherical aberration was determined as the major axis of the ellipse formed by the peripheral rays in the plane of paraxial focus.

A separate simulation modeled ray propagation at a planar twin grain boundary. The top grain ($z > 0$) was oriented such that $[001]_{ar} \parallel [121]_{lab}$ and $[100]_{ar} \parallel [\bar{3}11]_{lab}$. The bottom grain's lattice was rotated 64° counterclockwise around the $[001]_{ar}$ axis of the first grain. Rays of light are generated in the top crystal at azimuthal and elevation angles from -85° to 85° with a 20° step size. Each ray is modeled twice: once given that the ray is in its high eigenstate and once in the low eigenstate. Rays are traced through the surface and refracted into high and low eigenstates.

2.6 Transmitting Light

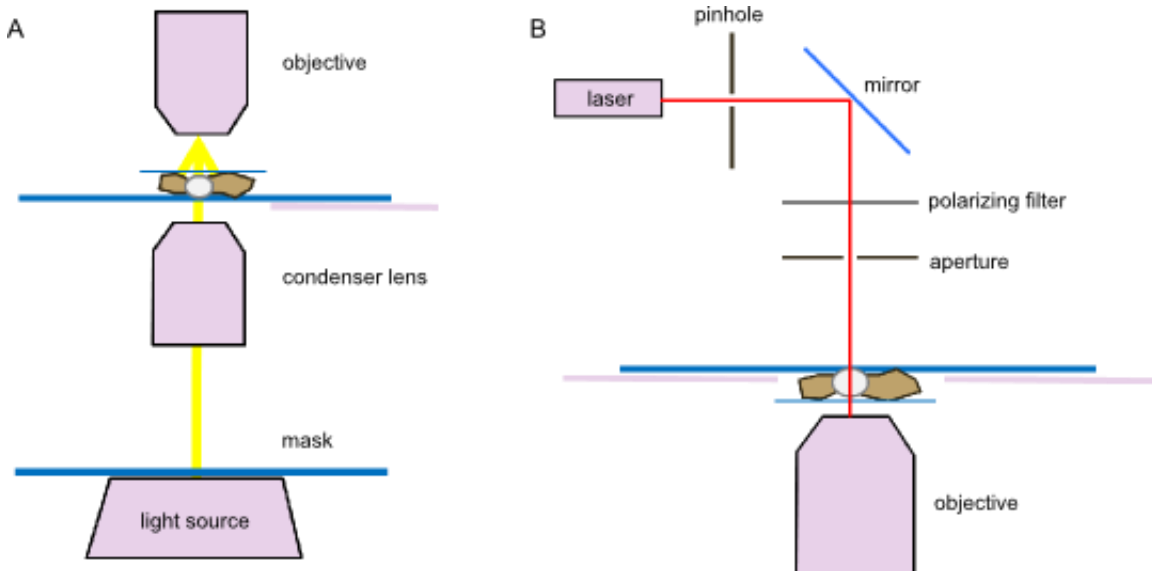


Figure 4. Diagram of ray tracing microscope setups.

2.6.1 Polarized Light

Isolated lenses were placed between cross polarizers and viewed using transmitted light microscopy in a Leica DM4000 upright light microscope. The sample stage was rotated to demonstrate changes in illumination.

2.6.2 Image Transmission

Images were transmitted through lenses on a Leica DM4000 upright light microscope. A mask was created by painting a glass slide with opaque nail polish and carving an “N” shape into the dried paint. The mask was placed between the microscope light source and the objective lens. Using Kohler alignment, the “N” image was focused below the ocellus lens such that the entire microscope field of view was evenly illuminated (Figure 4A).

2.6.3 Ray Transmission

A PASCO Scientific OS-8525 diode laser ($\lambda = 660\text{-}680\text{ nm}$) was aligned to pass through a pinhole, reflect off of a mirror tilted 45° relative to the laser path, and pass through a polarizing filter and an aperture before passing through an ocellus into the objective of a Leica DMI8 inverted light microscope (Figure 4B).

Image stacks were captured using a step size of $1\text{ }\mu\text{m}$, from $100\text{ }\mu\text{m}$ above the bottom of the lens to $100\text{ }\mu\text{m}$ below the bottom of the lens. Stacks were processed using MATLAB. Focal points were measured by iterating through stack slices, finding the centroid of all non-zero pixels in each slice, weighted by intensity, and finding the root mean square distance between non-zero pixels and the centroid, weighted by intensity. The plane with the smallest root mean square distance is the focal point, and the root mean square distance of that plane represents transverse aberration.

Projections of stacks were collected by calculating the sums of intensities along the projected direction and normalizing the intensities. Lines were detected in projections using a modified Hough transform^[41], described in Figure 5. Intersections were found between all rays in each projection. Intersections whose z-values were present only in one image were eliminated, as they would represent a false intersection between skew rays. While this method also eliminates sets of rays whose angle was not large enough to be detected in both projections, the multitude of false positives eliminated is larger than the number of false negatives generated. Longitudinal aberration was measured as the difference between the highest and lowest ray intersections.

```
transform = 2D array;
for each pixel (i,j)
    for t from 1 to 180
        var = i*cos(t) + j*sin(t);
        transform(t, var)++;
    end
end

newImage = 0;
thresh1 = 1;
thresh2 = 0.99;
newDiff = oldDiff = mean(oldImage - newImage);
while (newDiff>threshold && count<50000)
    oldDiff = newDiff;
    lines = select(transform, >thresh1 && <thresh2);
    plot lines on newimage and normalize;
    thresh1 = thresh2;
    thresh2 = 1 - 2*(1-thresh2);
    newDiff = mean(oldImage - newImage);
end
```

Figure 5. Pseudocode for modified Hough transform

3 Formation of the Lens

3.1 Microstructure

Studying the microstructure of the lens has a dual purpose – to explain the performance of the lens and to provide clues about the formation of the lens. In previous work, Speiser, et. al. proposed that the birefringence of the lens could lend the lens a dual focal length – one which would land in the rhabdom when the chiton is underwater and another which would land in the rhabdom when the chiton is on dry land.^[10] However, this premise would only hold if the lens is a single crystal with its lattice optic axis skewed from the lens optical axis (Section 4.1). Through electron backscatter diffraction (EBSD), we find that the lens is polycrystalline with traits which make it similar to a single crystal, with a lattice optic axis skewed from the lens optical axis.

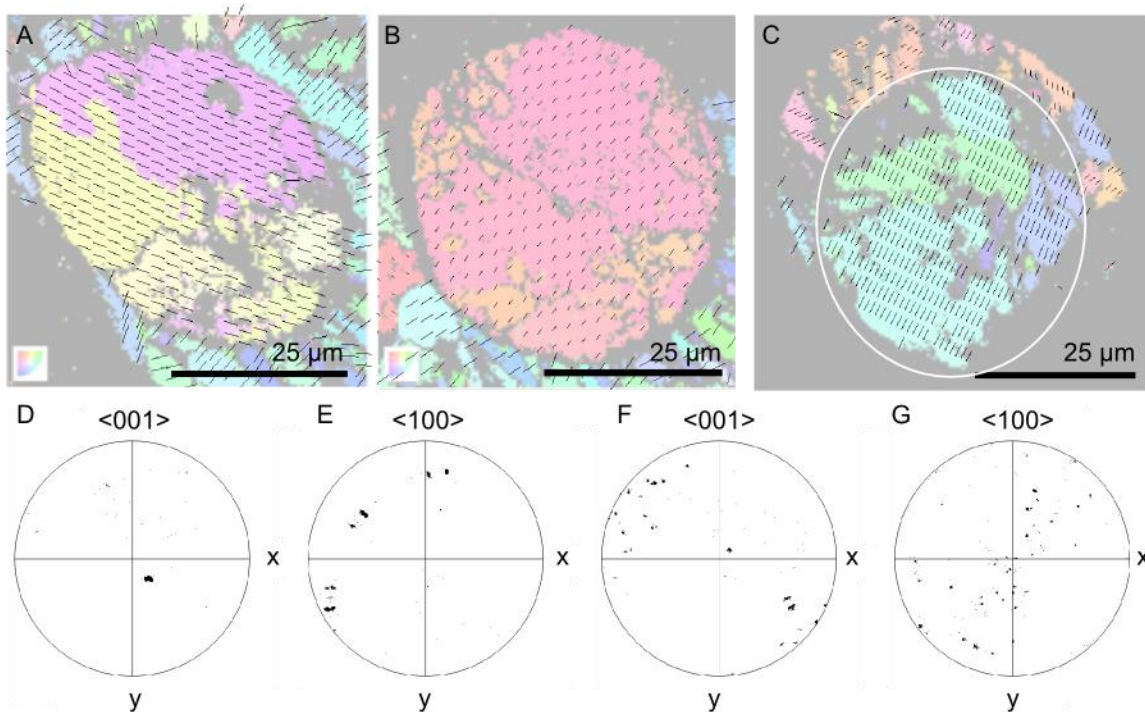


Figure 6. A-C) EBSD inverse pole figure (001)-axis maps. (001)-axis vector line segments are projected onto the lab x-y plane. A-B) Plan sections. C) Cross-section. White ellipse indicates location of lens. D-E) Pole figures from lens in (B). F-G) Pole figures from shell in (B).

3.1.1 Lens, shell, and cornea are composed of polycrystalline aragonite

EBSD maps demonstrate the lenses are polycrystalline (Figure 6). Inverse pole figure maps of the crystal (001) axis show that the crystallographic orientations of lenses are distinct from the neighboring shell (Figure 6A,B). A clear difference between the lens and the shell can be seen through the orientation of the (001) axis. The (001) axis exhibits a consistent orientation across the lens (Figure 6A-D), while the (001) axis is scattered in the shell (Figure 6A-C, F). Additionally, the orientation of the (001) axis is not continuous across the lens-shell interface.

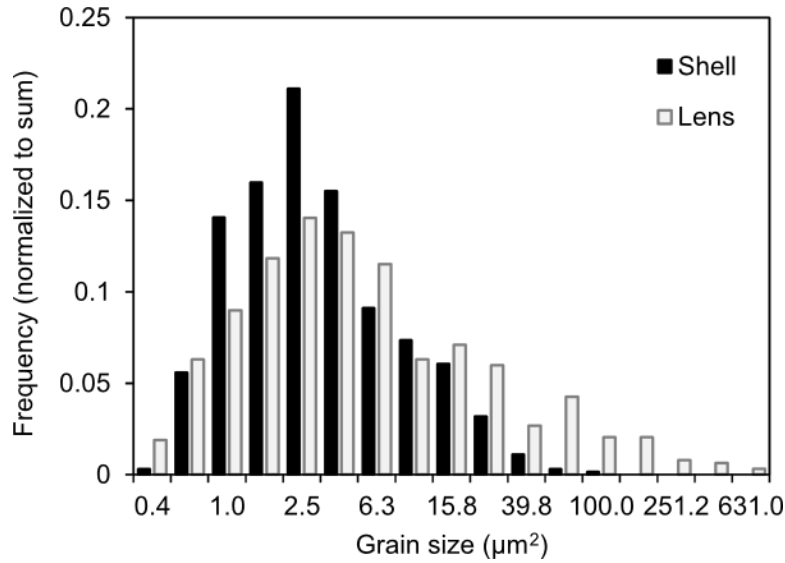


Figure 7. Sizes of grains in the lens and shell.

While all lenses are polycrystalline, grain sizes vary across lenses. Some lenses appear nearly single-crystalline, with one grain as large as 80% of the lens cross-section, while other lenses are composed of many smaller grains, with the largest grain composing only 19% of the lens cross-section. Usually, lens sections are dominated by 2-4 grains which take up over 90% of the lens cross-sectional area.

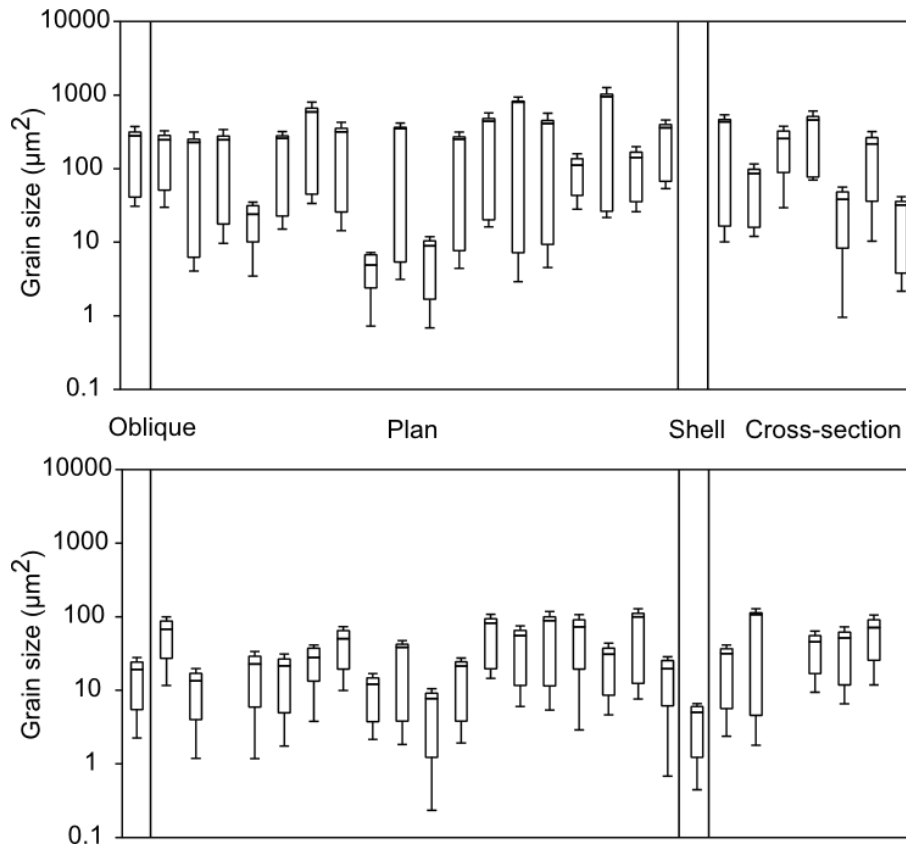


Figure 8. Sizes of grains in the lens (top) and shell (bottom)

Grains in the lens are larger than grains in the shell, as grains in the lens have a median cross-sectional area of $5.07 \mu\text{m}^2$, while grains in the shell have a median cross-sectional area of $3.24 \mu\text{m}^2$. Across all samples, grain sizes follow a log normal distribution in both the lens and the shell (Figure 7). The distribution of sizes in the lens is wider than the distribution for the shell due to the multitude of large grains in the lens. Furthermore, each sample exhibits a wide range of grain sizes (Figure 8).

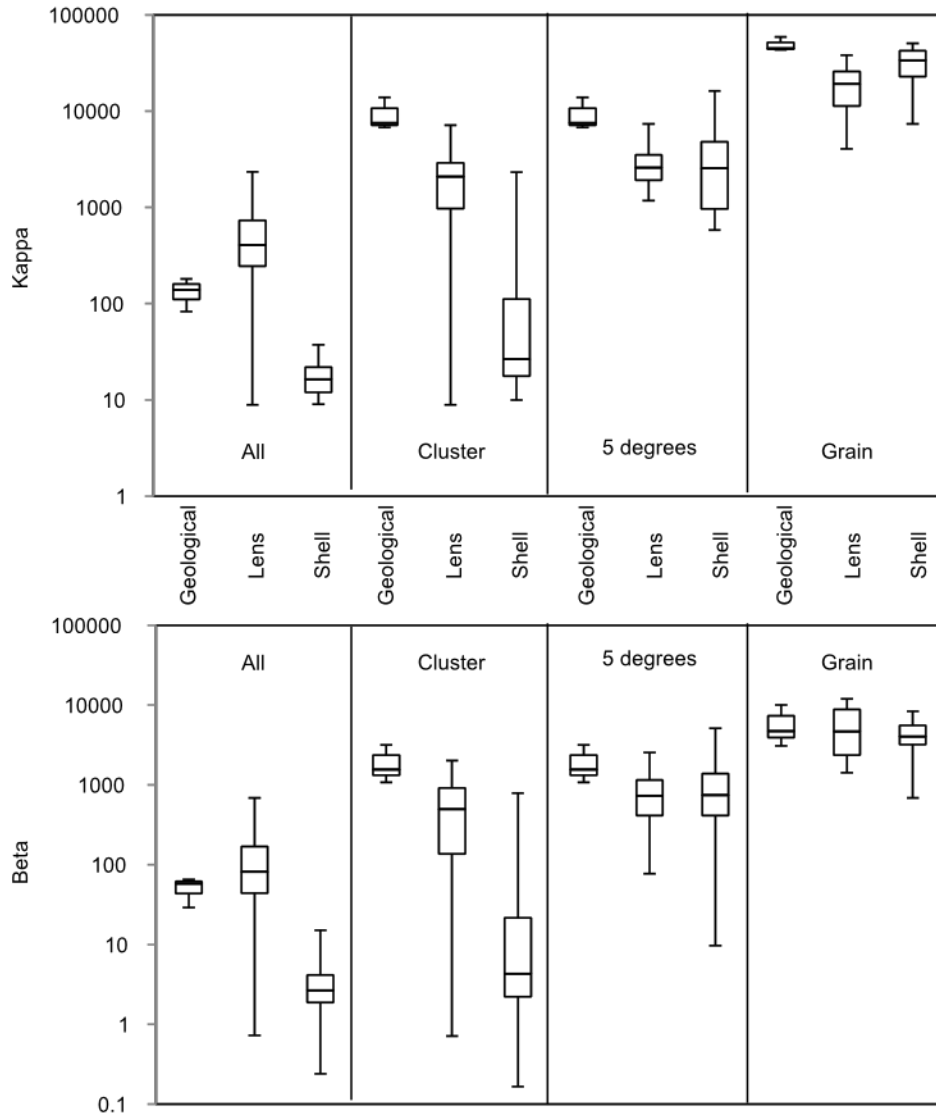


Figure 9. Kent distribution κ and β values for $\langle 001 \rangle$ axes, found using four methods

Variations in grain size and morphology may be a reflection of the diversity of microstructures between lenses. Additionally, each cross-section was taken at a different depth and angle in the lens, so variations may illustrate changes in microstructure at different points in the lens. However, there is no correlation between the relative sizes of large grains and total size of the cross-sections. This suggests that the grain size does not depend on proximity to the center of the lens. Examination of EBSD maps shows that in most lenses, large grains are not centered in the lens. Instead, they often extend from the edge towards the

center of the lens. While in most lenses there is no obvious texture, with small grains interspersed with larger ones (Figure 6a-c), in some, grains appear to fan out from a point of origin (Figure 14a-b). It is possible that this is a common feature, but is only detected when the section runs sufficiently close to this origin. The fan-shaped morphology suggests that there may be a single nucleation point upon which all grains grow.

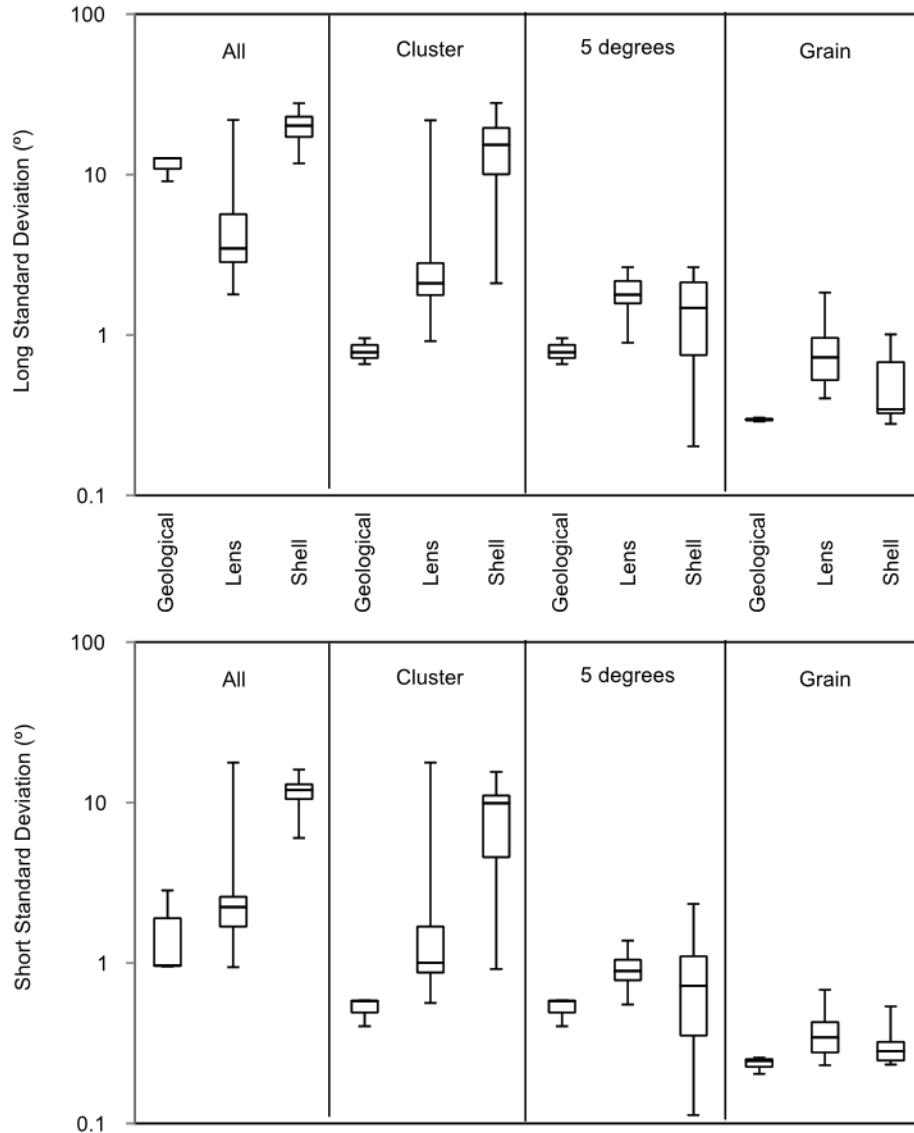


Figure 10. Standard deviations of Kent distributions, found using four methods

3.1.2 Grains are aligned in lens, cornea, and shell

In all sections, pole figures indicate that $\langle 001 \rangle$ axes are highly aligned (Figure 6). Axes exhibit a clear, dense cluster at a specific point, with some extra points dispersed across various orientations (Figure 6D). Non-aligned points appear both in noisy scans and in scans with consistently high band indexing confidence.

3.1.2.1 Kent Distributions of $\langle 001 \rangle$ axes

Kent distributions describe distributions of vectors primarily using two parameters: κ and β . The parameter κ describes how narrow the distribution is, and β describes how elliptical the distributions are. For clarity, standard deviations along the least dense and densest directions are also reported here. $\langle 001 \rangle$ axis orientations were fit to Kent distributions using four methods: including all points, including points selected using Mathematica's FindClusters function, including points within 5° of the cluster centroid, and points within the largest grain in the sample. Points were not cleaned or extrapolated before fitting.

As expected, distributions of dominant clusters in the lens are tighter than the distributions of all points in the lens (Figure 9, Figure 10). Clustering and the 5° threshold have nearly equivalent effects, though the threshold skews the distribution to appear narrower for the shell, which does not exhibit a clear, singular cluster (Figure 6F, Figure 9, Figure 10). Selected subsets exhibit higher κ values and lower standard deviations than the set of all points in the lens because of the difference between the cohesive cluster of $\langle 001 \rangle$ axes in the lens and the outliers. The outliers have a significant enough presence to increase the long standard deviation of the distribution by a factor of 2, from the 5° threshold method to the all-point method (Figure 10). The grains contributing to these outliers are small, and some may be incorrectly indexed points, but the outliers which do exist will hinder the performance of the lens and contribute to inconsistent refractive indices throughout the lens.

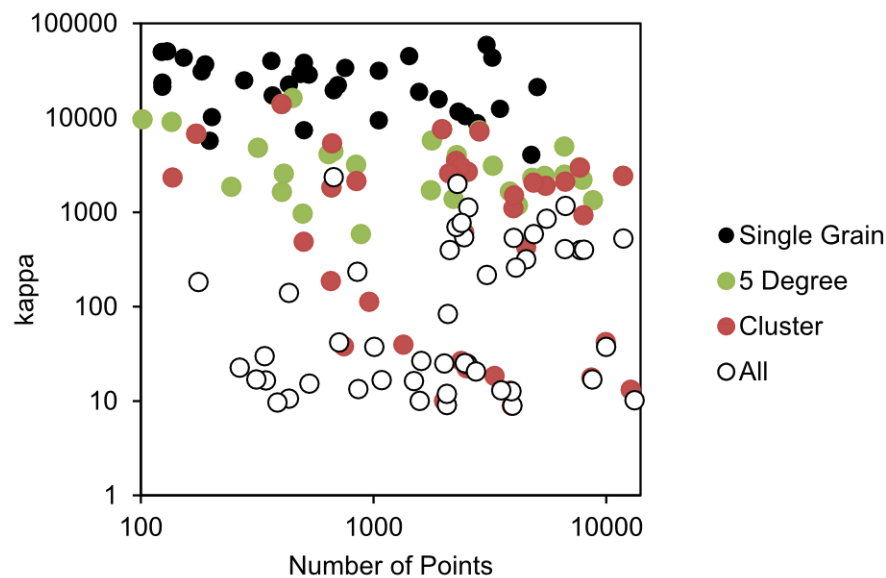


Figure 11. Lack of correlation between number of points included in distribution and size of the distribution.

Points within single grains exhibit narrow distributions. Despite the critical disorientation of 1° used to define a grain, $\langle 001 \rangle$ axes in the lens in some samples have long standard deviations over 1° (Figure 10). This reflects a gradual change in angle across the grain, which would correspond to low angle grain boundaries. Kent distributions of points within single grains in the geological crystal have the highest κ values and lowest standard deviations, indicating that the geological crystal has few defects. Some instrumental broadening is expected, so it is unknown precisely how large the actual spread of the $\langle 001 \rangle$ axes is in the geological crystal. In contrast, grains in the lens and shell, though exhibiting a wider range of κ values and standard deviations, have higher standard deviations and lower κ values, indicating that

grains in the lens and shell contain defects that impact the orientation of the $\langle 001 \rangle$ axis. Though the median lens distribution is wider than the median shell distribution, the two are statistically equal, indicating no conclusive difference between defect concentrations in the lens and shell (Figure 9, Figure 10).

In all methods and samples, β values are consistently high and follow κ , representing unimodal distributions (Figure 9). The high ellipticity is a consequence of the high concentration of the points, rather than a considerable asymmetry. In most cases, the long standard deviation is roughly twice the short standard deviation. This slight ellipticity may be a consequence of poor $\langle 001 \rangle$ consistency across low angle grain boundaries, preferential deviation of the $\langle 001 \rangle$ axis along certain directions in aragonite twinning, or a predilection for dislocations and impurities to line up with specific planes.

3.1.2.2 Absolute orientation of the $\langle 001 \rangle$ axis

While the $\langle 001 \rangle$ axes of grains within any given lens are highly aligned, the $\langle 001 \rangle$ axis is tilted away from the lens optical axis by $12^\circ - 82^\circ$. Some uncertainty is expected in the determination of the lens optical axis, as the orientation of the optical axis was determined from cross-sectional shape and position of the pigmentation. However, it is clear that the $\langle 001 \rangle$ axis is not aligned with the lens optical axis, defying the motif seen in trilobite and brittlestar lenses, where the calcite $\langle 001 \rangle$ axis is oriented vertically along the lens optical axis.^[17,20] Thus, we reveal a second distinct difference between the chiton ocelli lens and other mineralized lenses, aside from its aragonitic composition. In the other lenses, the calcite $\langle 001 \rangle$ axis, which is also the calcite optic axis, points upwards out of the lens, extinguishing birefringence for light which travels vertically along the lens optical axis. In ocelli lenses, neither the $\langle 001 \rangle$ axis nor the crystallographic optic axis is oriented along the lens optical axis, such that birefringence cannot be extinguished fully, and the minimum birefringence occurs when light travels at an angle towards the lens.

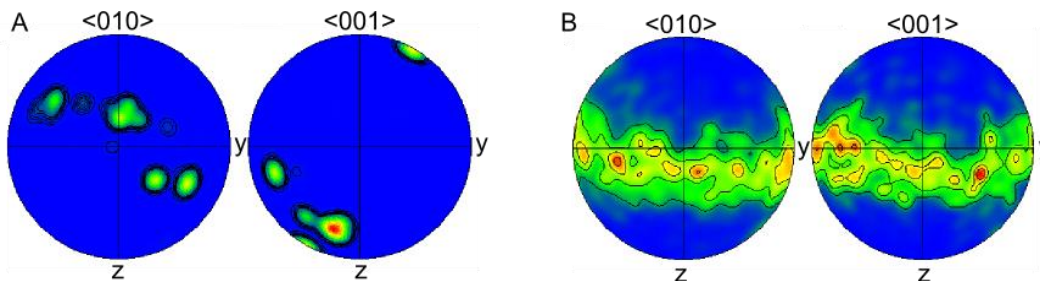


Figure 12. Contoured pole figures for cornea (A) and shell (B).

Distributions vary between classes of samples. The geological crystal exhibits the narrowest distribution for all subset methods, but it exhibits less alignment than the lens when all points are taken into account. In multi-grain analyses, the Kent distributions of points in the shell are wider than distributions of points in the lens and geological crystal. Because the lens has a much stronger $\langle 001 \rangle$ axis alignment than the shell, it is more capable of optically mimicking a single crystal. While distributions for the geological crystal included the most points, and distributions for the shell included the least points, there is no correlation between Kent distribution width and number of points included (Figure 11).

Like the lens, the cornea is polycrystalline. The average cornea has a center thickness of $6.94 \pm 1.87 \mu\text{m}$ ($N=5$), and the cornea thickness increases as it approaches the shell. While $\langle 001 \rangle$ axes in the cornea exhibit some clustering, the $\langle 001 \rangle$ axes in the cornea are more disperse than the $\langle 001 \rangle$ axes in the lens, and

the $\langle 100 \rangle$ and $\langle 010 \rangle$ axes do not demonstrate any alignment (Figure 12A). Likewise, pole figures of the shell show significant spreading of the $\langle 100 \rangle$, $\langle 010 \rangle$, and $\langle 001 \rangle$ axes, demonstrating a lack of alignment (Figure 12B).

3.1.2.3 Non-aligned axes

The $\langle 100 \rangle$ and $\langle 010 \rangle$ axes (which are complementary) show some clustering in samples dominated by a few grains (Figure 6E). However, the number of clusters is not statistically correlated with the number of large grains in the lens; rather, many small grains contribute to larger clusters. These small grains are not always in the same part of the lens. In many cases, non-adjacent and sometimes distant sections of the lens exhibit the same crystallographic orientation (Figure 6A-C).

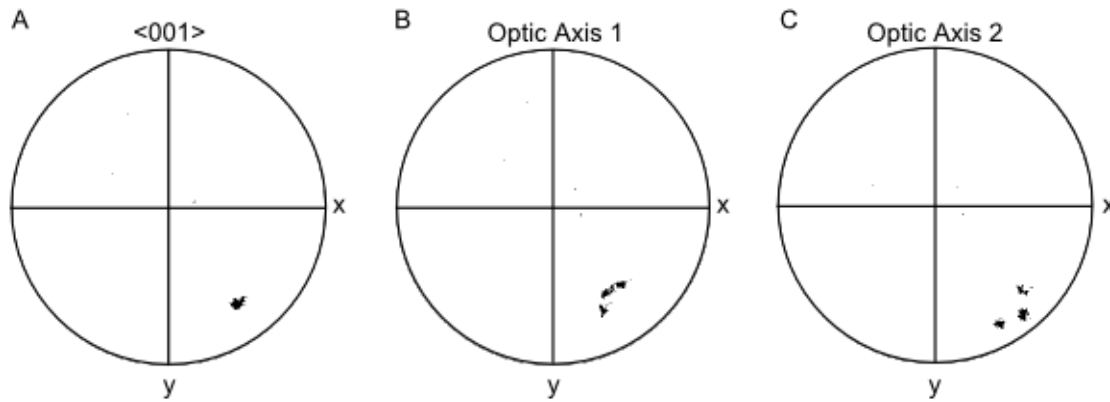


Figure 13. Pole figures for plan section.

The optic axes, like the $\langle 100 \rangle$ and $\langle 010 \rangle$ axes, are not clustered and form small rings around the tightly aligned $\langle 001 \rangle$ axis (Figure 13B). Birefringence is extinguished along the optic axes rather than the $\langle 001 \rangle$ axis. Because the $\langle 001 \rangle$ axis is aligned instead of the optic axes, the lens has no direction along which birefringence is entirely extinguished. However, birefringence will be limited because the $\langle 001 \rangle$ axis is close to the optic axes.

3.1.3 Twinning is prevalent in the lens

Table 2. Kent distributions of misorientation axes for given misorientation angles, within 1°

Misorientation Angle ($^\circ$)	N	κ	β	Angle between mean and $\langle 001 \rangle$ ($^\circ$)
12	1091	47.54	3.16	0.88
28	35	3.35	0.50	13.50
54	224	12.59	0.47	1.64
64	4791	153.24	6.73	0.06
72	213	1.20	0.01	7.42
90	186	1.24	0.01	28.66
104	216	1.81	0.06	11.36

Orientation relationships between neighboring grains were determined by finding an axis and angle of rotation about that axis that superposes the two lattices. The probability distribution of the misorientation angle calculated for all lens, shell, and cornea samples shows a sharp maximum at 64° , with $\langle 001 \rangle$ as axis of rotation (Figure 14D,E).

The tight Kent distribution of misorientation axes confirms that the dominant axis is the $\langle 001 \rangle$ (Figure 14D). This is consistent with twinning on the $\{110\}$ and $\{1\bar{1}0\}$ planes¹ (axis $\langle 001 \rangle$, angle 63.75°), a common feature of crossed-lamellar aragonite structures like the *A. granulata* shell.^[42] However, unlike the planar and cyclic twinning seen in geologic and biogenic aragonites, the twin boundaries in ocelli exhibit high curvature (Figure 6A, Figure 14A) and may therefore be incoherent. While cyclic twinning is common in geological aragonites^[43,44], the fan-shaped morphology in ocelli lenses results from a combination of twins and low-angle grain boundaries rather than cyclic twins (Figure 14B).

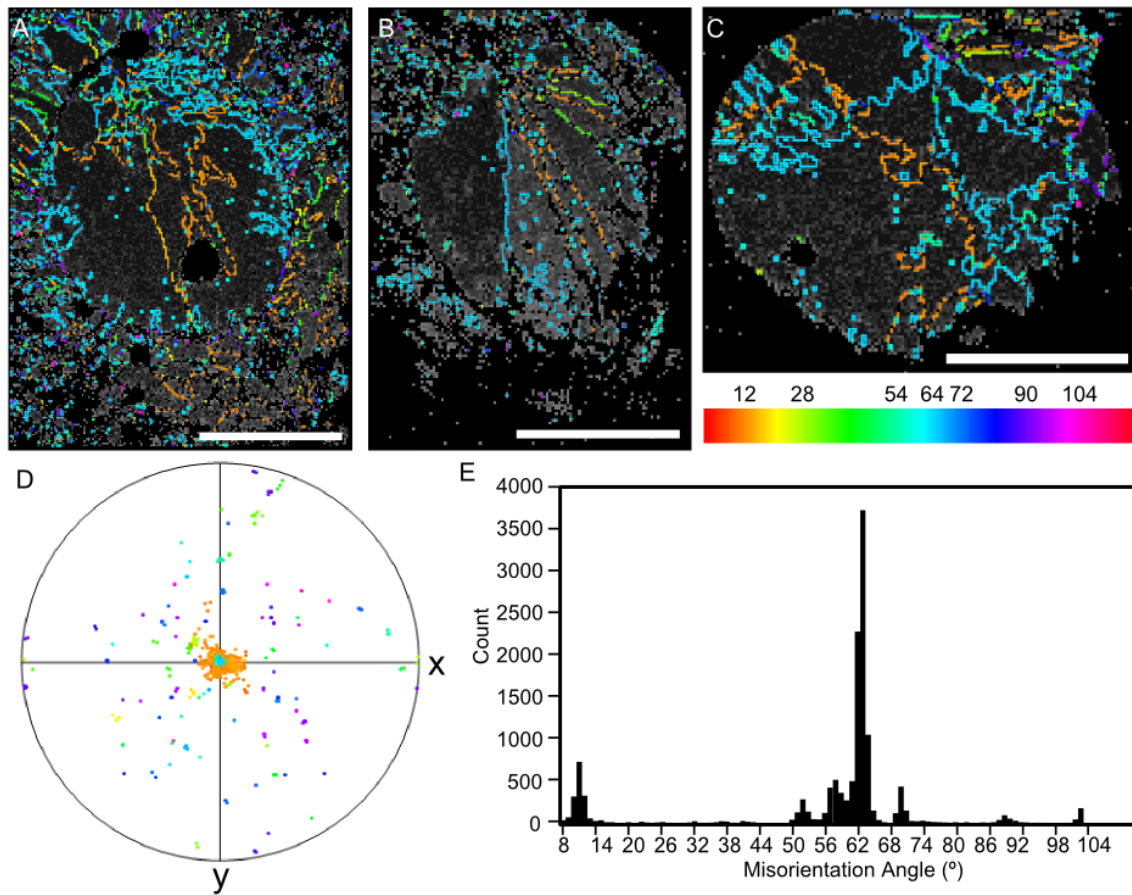


Figure 14. Misorientation between neighboring grains. A-C) Misorientation angles displayed on band contrast maps. Line colors indicate misorientation angles. A-B) Plan sections in shell. C) Cross-section. D) Pole figures of misorientation axes in (C). E) Histogram of misorientation angles in lens, shell, and cornea across all samples. Scale bars 20 μm . Scans A-C by Lyle Gordon.

¹ In the Pmmm space group, $\{110\}$ and $\{1\bar{1}0\}$ are equivalent through symmetry. Aragonite belongs to the Pmcn space group, in which $\{110\}$ and $\{1\bar{1}0\}$ are distinct. In misorientation calculations, Oxford hkl software and our own code use orthorhombic Pmmm symmetry (space group #47) instead of Pmcn symmetry (space group #62) operators. Therefore, in our own calculations, $\{110\}$ and $\{1\bar{1}0\}$ are equivalent, but in experimental conditions, twinning on the two planes would be distinct.

In addition to the maximum at 64°, smaller maxima in the misorientation angle distribution occur at 12°, 28°, 54°, 72°, 90°, and 104° (Table 2). Kent distributions of misorientation axes collected from all lens, shell, and cornea grain boundaries show that misorientation axes for 64° and 12° grain boundaries are sharply aligned on the $\langle 001 \rangle$ axis, while other angles produce looser distributions with means that deviate from the $\langle 001 \rangle$ axis (Table 2, Figure 14D). Misorientation axes are most sharply aligned to the $\langle 001 \rangle$ axis for 64° grain boundaries. The loose maintenance of $\langle 001 \rangle$ axes for the prevalent 12° grain boundaries explains why $\langle 001 \rangle$ axes in lenses exhibit wider distributions than $\langle 001 \rangle$ axes in the geological crystal. Not only does the lens possess more twin grain boundaries which slightly spread the $\langle 001 \rangle$ axis, the lens contains many low angle grain boundaries which spread the $\langle 001 \rangle$ axis more than the twinned boundaries in the geological crystal.

Some lenses are dominated by 64° misorientation angles, while other sections have a large presence of low-angle boundaries (Figure 14A-C). This variation may originate from the different depths and angles at which the sections were collected.

3.2 Impurities

Impurities are critical for the formation of biominerals^[27,31]. Magnesium supports the formation of aragonite, and other impurities common in tidepools such as sodium and strontium may impact the microstructure and shape of the crystal. Common organic impurities in calcium carbonate-based minerals include aspartic acid-rich proteins, glutamic acid-rich glycoproteins, and polysaccharides^[31,45]. Here we locate impurities in chiton ocelli lenses, with some indications of the class of the impurities, between metallic ions, organic macromolecules, and amorphous calcium carbonate (ACC).

3.2.1 The lens-shell interface contains organic matter

Energy dispersive spectroscopy (EDS) line scans indicate an increase in oxygen and carbon content coupled with a decrease in calcium content at the border between the lens and the shell (Figure 15). Although calcium and oxygen are both present in aragonite, a disproportionate amount of calcium and oxygen could indicate the presence of organic components. The increase in organic elements could come from large concentrations of proteins or polysaccharides at the lens-shell border.

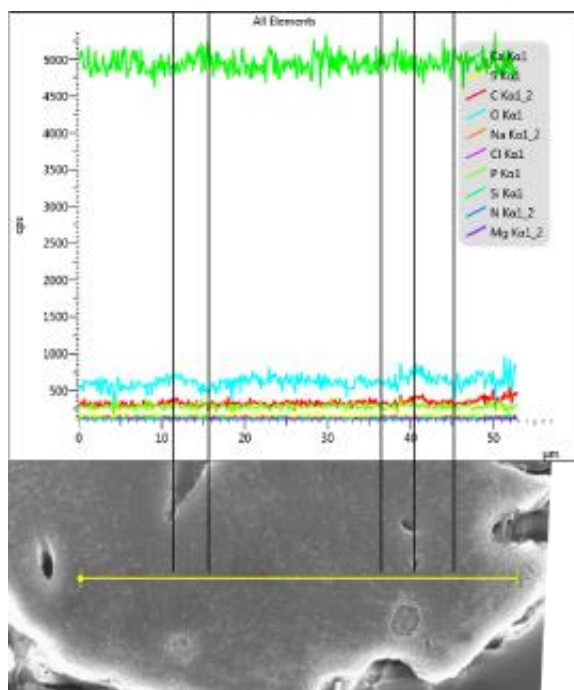


Figure 15. EDS line scan through lens. Simultaneous oxygen and carbon peaks and calcium depressions are visible at lens-shell interface.

Etched lenses support the EDS spectra, showing fast etching rates at the interface between lens and shell (Figure 16B). While cation impurities like magnesium or sodium could also contribute to increased etching rates, the EDS spectra do not indicate an increase in cation concentration at the lens-shell interface. However, EDS usually exhibits minimal signal for magnesium and sodium, so further work such as wavelength dispersive spectroscopy (WDS) or tip-enhanced Raman spectroscopy (TERS) is necessary to identify those elements in lenses.

A high misorientation between the lens and the shell would cause a fast etching rate at the lens-shell interface. However, EBSD scans show that some twin grain boundaries are continuous across the lens-shell interface (Figure 14A), while other twin grain boundaries exist between the lens and the shell (Figure 14C). Because the twin density is no greater at the lens-shell interface than within the lens or shell, the lens-shell interface should not etch quickly purely because of misorientation. Thus, it is likely that the interface contains a high concentration of impurities.

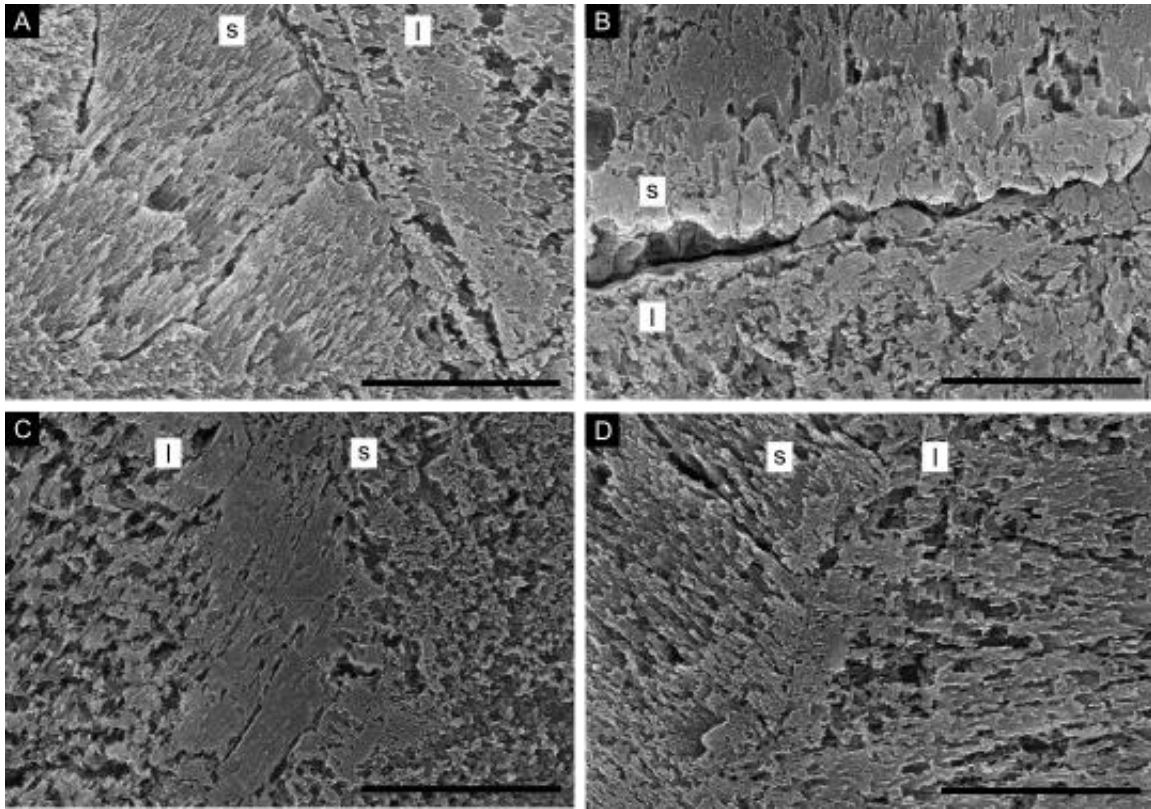


Figure 16. SEM micrographs of etched lens-shell interfaces. Scale bars 2 μm . “s” shell, “l” lens.

Etching rates vary greatly from interface to interface. In several regions, the lens etching pattern appears to be isotropic near the lens-shell interface (Figure 16B,C). In some areas, bands bunch closely at the lens-shell interface, dominating the etching structure (Figure 16A). In other regions, etch pits run perpendicular to the lens-shell interface, producing curved projections which extend outwards from the interface (Figure 16D).

Likewise, the shell exhibits a diversity of structures at the lens-shell interface. Some shell segments appear to be a reflection of the projections in the lens which appear to extend outwards from the lens-shell interface (Figure 16D). Though the three-dimensional orientation between the projections cannot be measured using SEM, the angle between the projections in the lens and shell could be 64° , indicating that the two paired patterns are a result of twinning at the lens-shell interface. Some shell segments portray the opposite pattern, where the projections appear to extend towards the interface rather than away from it. Other shell segments appear to be a reflection of the amorphous nature of the lens etching pattern (Figure 16B,C).

Etching rates at the lens-shell interface vary. At some sites, the entire lens-shell interface etches deeply (Figure 16A,B), which could be a result of misorientation or impurities. At other sites, the lens-shell interface etches less than the lens or shell (Figure 16C), which could represent a lack of impurities or strong crystallographic alignment. Most interfaces reflect a moderate etching rate, leaving a mild valley between the lens and the shell (Figure 16D). The variety in interfaces could be a result of the variety of misorientations that exist across the lens-shell interface, or it could come from discrepancies in growth rates which deposit varying amounts of impurities at the edge of the lens.

3.2.2 Bands demonstrate the direction of growth

Faint, dark elliptical bands are located near the bottom of the lenses in BSE images (Figure 17A,B). These bands indicate that low-atomic number layers are present in the lens. The layers could be low-Z impurities like sodium or magnesium, or they could be composed of organic matter.

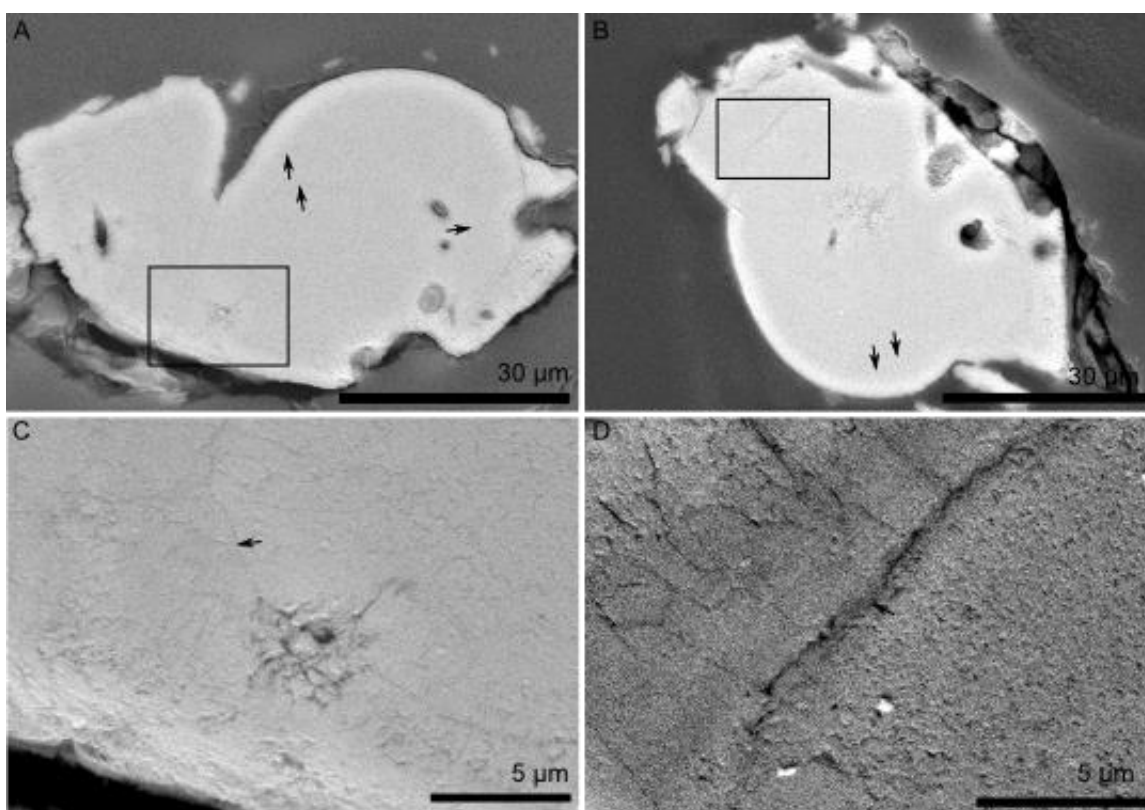


Figure 17. Backscattered electron SEM micrographs of polished, coated lens cross-sections. A-B) Cross-sections. Boxed regions indicated locations of (C-D). Arrows indicate dark bands. C-D) Regions of cross-sections. Black lines indicate the lens-shell interface.

Etched samples also show thin elliptical etched bands radiating from a central point, both for cross-sections and plan sections (Figure 18, Figure 19). Band thicknesses and frequencies vary. Near the shell, bands tend to be thinner and closer together, while aragonite bands are wider near the core. The core of the band structure is the thickest layer in the pattern. Only one sample out of 24 characterized using EBSD demonstrated a banded microstructural pattern similar to the etching patterns (Figure 18A,B). Because the microstructure of ocelli rarely matches the banded structure shown in etched samples, the etching is due to bands of impurities, rather than grain boundaries.

Although grains in the lens do not match the morphology of growth bands, the grains do have a unique relationship with the bands. In EBSD scans of lenses, a fan-shaped morphology can often be observed, where many large grains extend from a central point at the core of the band structure towards the edge of the shell (Figure 18B,F).

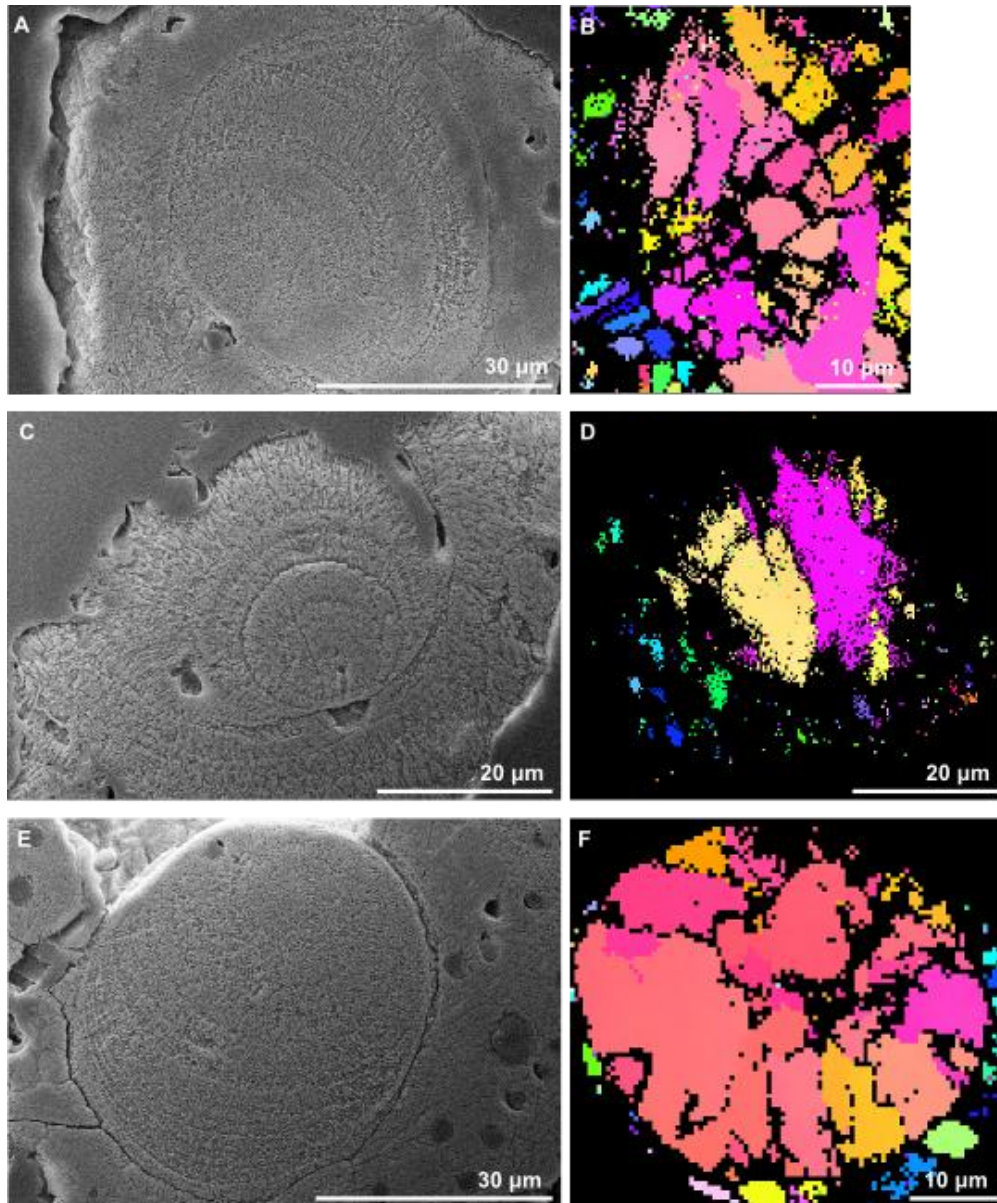


Figure 18. Etched plan sections of ocelli with corresponding EBSD inverse pole figure z-axis maps.

In optical micrographs of ocelli, faint, thin dark bands can be seen (Figure 19). Like the etching bands, these dark bands are variable in thickness and have a similar contour to the edge of the lens, indicating that the bands represent growth layers within the lens. The bands shown in optical micrographs match etching bands shown in SEM micrographs (Figure 19C-F). Dark, thick bands can be seen at the bottom of the lens in some optical micrographs. These bands translate into regions of densely packed, quickly etched bands (Figure 19).

Because magnesium, sodium, and strontium carbonates and ACC are white, the color in the bands could come from organic pigment. Bands tend to be more densely packed at the edge of the lens, adjacent to the pigmented shell (Figure 19). However, the colors of the bands in the lenses are not the same hue as the pigmented shell, which suggests that the composition of the bands is distinct from the pigment in the shell.

It is also worth noting that the core of the bands tends to be attached to the shell, while the lens-shell interface at the outer edge of the bands often fractures when lenses are extracted. The dense distribution of the bands at the edge of the lens could weaken the lens-shell interface, as the layers at the edge of the lens delaminate easily due to the high impurity concentration (Figure 19).

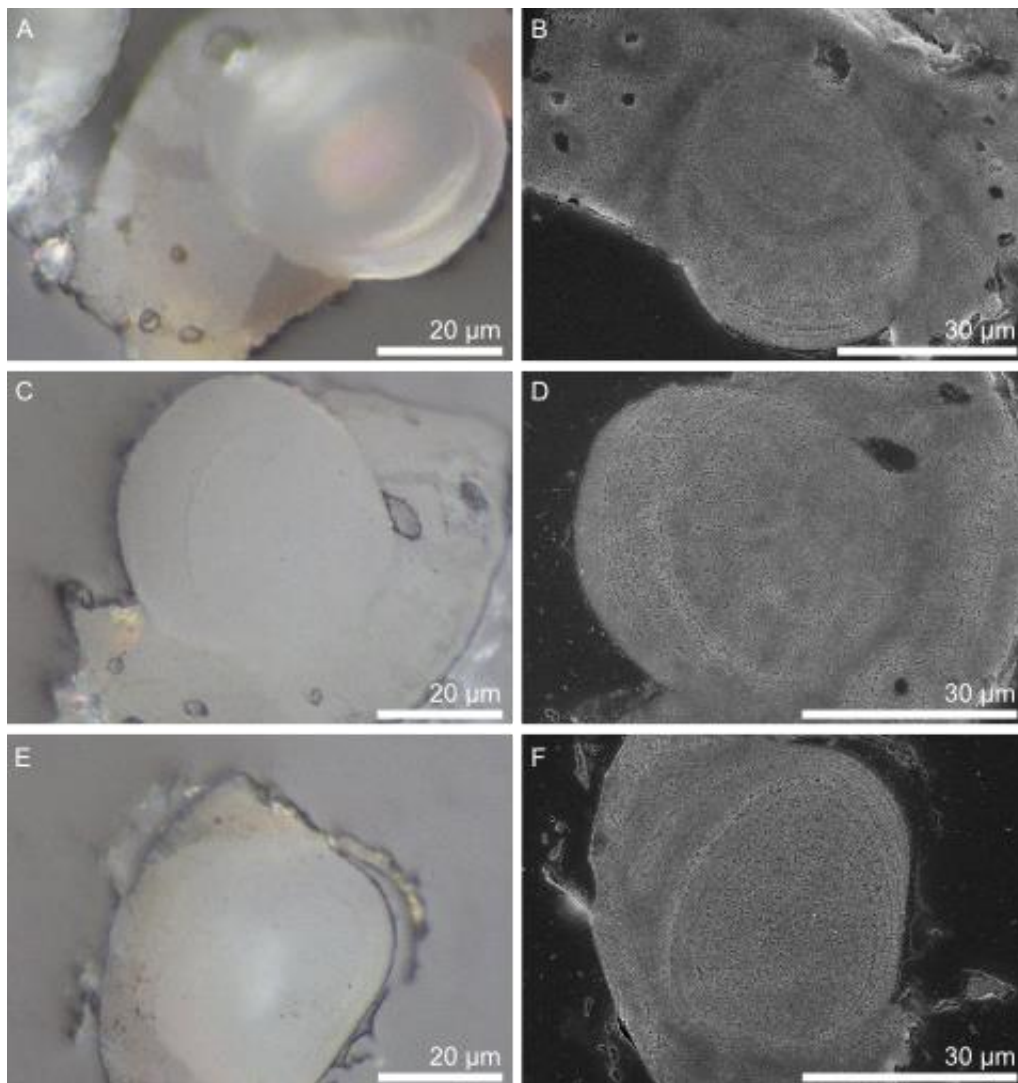


Figure 19. Optical micrographs and corresponding SEM images of etched lens plan sections.

3.2.3 Pores at the lens-shell interface indicate a potential nucleation point

In many lenses, growth bands and fanning grains converge on a point on the lens-shell interface that contains a pore (Figure 14A-B, Figure 18A,C, Figure 19A-B). The pore could be a microaesthete. Aesthetes in chitons function as sensory and secretory channels. Microaesthetes are prevalent near ocelli, and they often branch from the rhabdom to areas near the lens, but they do not touch the lens. While those microaesthetes may serve a light gathering function like the microaesthetes used by lensless chitons^[10], the microaesthete closest to the lens may serve a secretory function. The microaesthete could serve as a channel to transport materials to the lens before it is formed.

Alternatively, the pore could be self-contained. This appears to be the more likely solution, as the pore is typically larger than a microaesthete. Although a microaesthete would be seen in any cross-section, an isolated pore could only be found at certain cross-section depths. Because the inside of the pore is not mineralized, it is more likely to contain a packet of organic materials than ion impurities or ACC.

3.2.4 Regional compositional differences demonstrate impurity localization

SEM BSE micrographs do not indicate a drastic difference in composition between the lens and the shell (Figure 17A,B). Close inspection of the lens-shell interface shows that the shell is slightly darker than the lens, indicating that the shell is composed of lower-atomic number elements, the contrast is very small (Figure 17C,D). Likewise, the cornea does not show conclusive z-contrast with the shell or lens (Figure 17C).

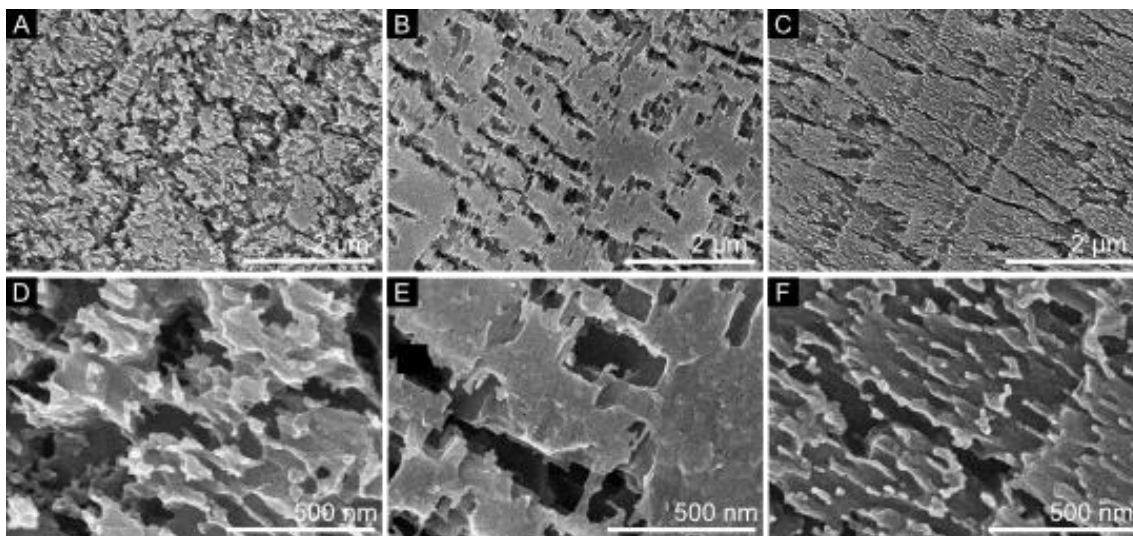


Figure 20. SEM micrographs of lens regions. A,D) Core of growth bands. B,E) Middle of lens without bands. C,F) Middle of lens with bands.

SEM micrographs of etched lenses indicate differences in etching rate between the core of the lens, the outer portions, and the shell. The core of the bands consists of fine granular structures with little coherent orientation (Figure 20A). Projections show some preferential etching based on orientation, indicating a possible link between impurities and crystallographic planes (Figure 20D).

In the outer lens, longer aragonite projections extend perpendicular to bands (Figure 20C,F). The projections vary in morphology between regions. In areas with few bands present, planes etch evenly, and

surface roughness is low (Figure 20E). In regions with few bands, etching reveals deep, sharp, rectangular etch pits on the order of 100-300 nm (Figure 20E). These pits could be evidence of interpenetrating twins common in crossed lamellar microstructures. The interpenetrating twins could be the reason why highly curved twin grain boundaries are visible in EBSD. On the scale of several microns, the boundaries may be curved, but at the scale of hundreds of nanometers, interpenetrating twins would break the large curved grain boundary into a series of smaller, flat interfaces. The prismatic etch pits could also be a consequence of the nanocrystal method of assembly, as small crystals surrounded by organic matrix may be removed entirely through dissolution of the organic matrix.

The non-banded regions exhibit distinctly different etching patterns from banded regions which exhibit high surface roughness and curved etch pits (Figure 20F). The curvature of the etch pits in the banded regions could indicate the presence of impurities which support the formation of curved surfaces. While etch pits in low-band regions are all elongated along the same direction (Figure 20B), the alignment of pits in the low-band regions is not as consistent as orientations in high-band regions (Figure 20C).

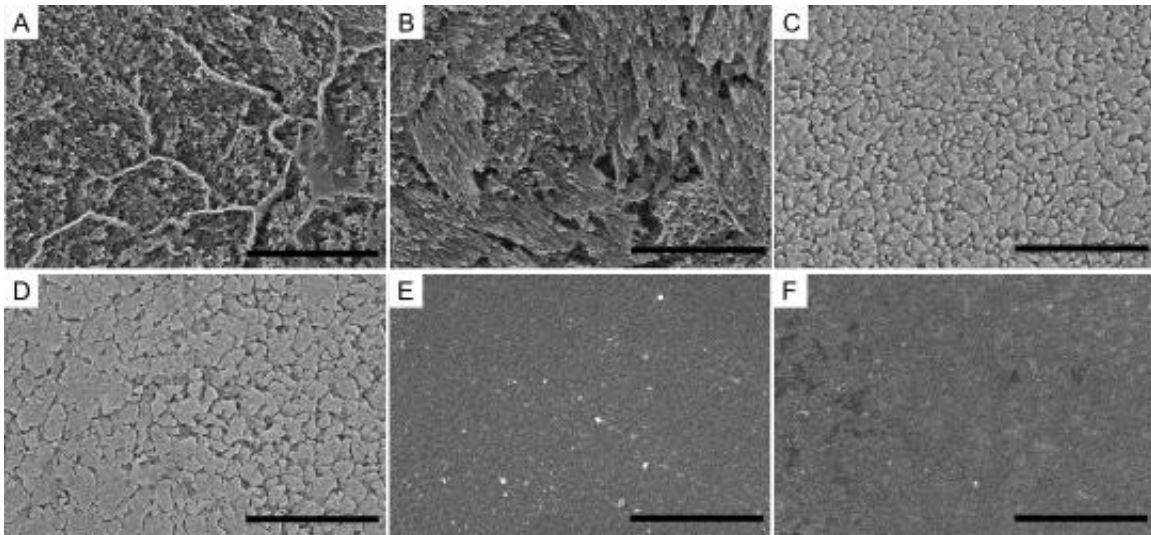


Figure 21. SEM micrographs of etched aragonite. A-B) Pigmented shell near ocellus. C) Articulum. D) Non-pigmented tegmentum. E) Shell viewed along (100) axis. F) Shell viewed along (001) axis. Scale bars 2 μm .

The core is sometimes attached to the cornea and other times attached to the shell, but it does not cover the entire cornea-lens or shell-lens interface. The cornea and shell have similar etching patterns to the aragonite bands in the lower portion of the lens, but the projections are less ordered and do not etch as deeply as the bands in the lens (Figure 21B). Near the lens-shell interface, some vermiculations extend towards the interface, bending away from the interface normal as they transition into the disordered shell pattern (Figure 16D).

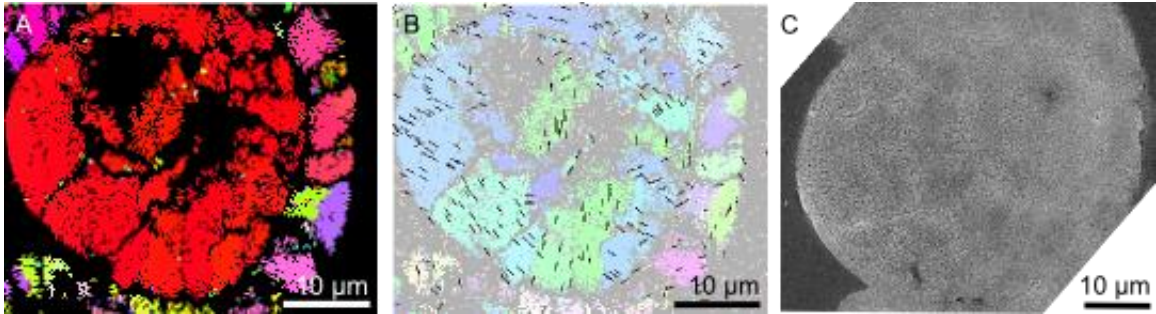


Figure 22. EBSD and etching of same lens. A) Inverse pole figure z-axis scan of polished lens. B) Inverse pole figure x-axis scan of polished lens with $\langle 100 \rangle$ axis vectors projected onto image. C) SEM micrograph of etched lens, surrounded partially by shell.

An EBSD scan of a lens which was etched, observed in SEM, and then re-polished reveals the relationship between crystallography and etching patterns. While the grains exhibit a fan-shaped microstructure that originates at the same origin of the growth bands, the orientations of the grains in the lens do not demonstrate a relationship with the growth bands (Figure 22B). Though etched regions of the growth bands exhibit finger-like projections which extend perpendicular to the bands, the $\langle 100 \rangle$ and $\langle 010 \rangle$ axes are neither parallel nor perpendicular to the growth bands (Figure 22B,C). Orientations of such axes appear to be more dependent on twinning than on the growth direction. Thus, the etching pattern depends on impurity orientation rather than crystallographic orientation.

3.3 X-ray microtomography

X-ray microtomography stacks demonstrate the three-dimensional morphology of the shell and ocelli without cutting into the sample, removing erosion artifacts from polishing. Fully-formed ocelli are clearly visible and appear to be nearly elliptical, with some asymmetry (Figure 23B,C). The cell cavity, likewise, is asymmetric. Rather than taking an elliptical shape, the cavity is pear-shaped, with the wide end near the ocellus and the narrow end tapering into an aesthete that diverges from the shell normal. The slant of the cell cavity coupled with the asymmetry of the lens will cause the focal point to not be centered in the cell cavity. Whether the chiton has the sensory capabilities to cope with the lack of symmetry is unknown.

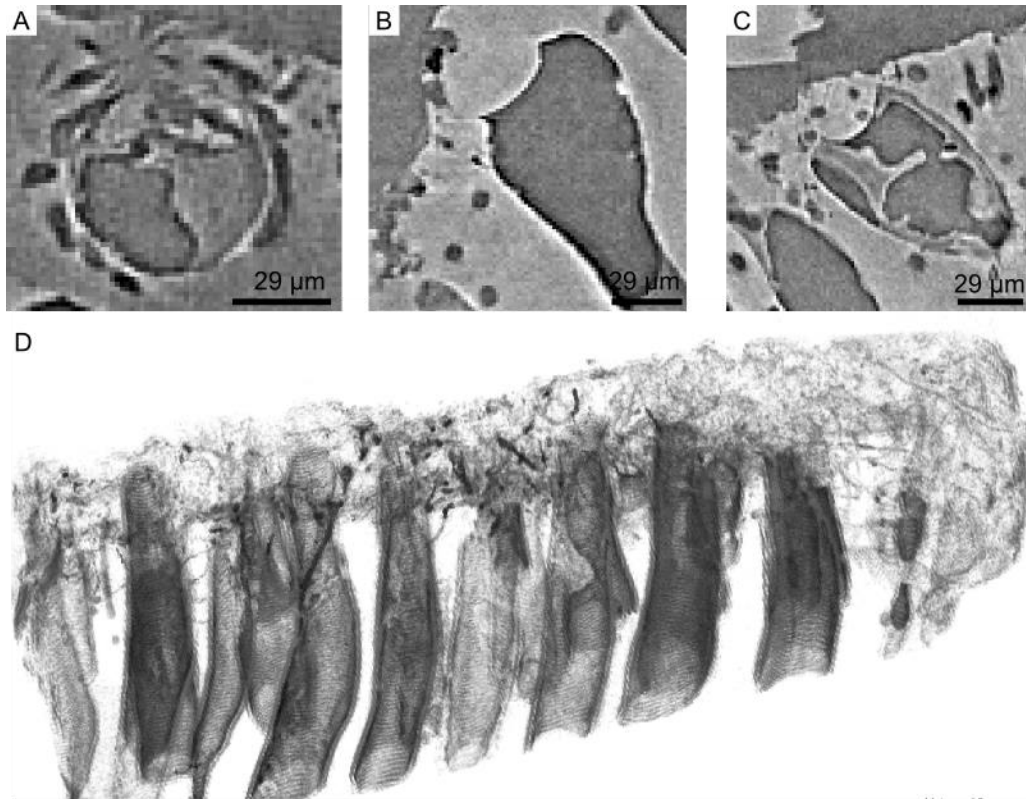


Figure 23. X-ray tomography of *A. granulata* valves. A) Cross-section of partially-formed ocellus. B,C) Cross-sections of fully-formed ocelli. D) Volume view of aesthetes. Scans by Dr. Stuart Stock.

For all lenses, microaesthetes run close to the lens, and many microaesthetes extend from the cell cavity to the shell surface (Figure 23A-C). In some cases, microaesthetes appear to run through the lens (Figure 23C). However, no channels have been found in cross-sections of lenses, so the channels seen in x-ray tomography may be an artifact or a consequence of high etching in the samples used for this method. Still, the channels may be naturally present in many lenses. Some lenses shattered during the extraction process used to create cross-sections, so those brittle lenses may be the porous lenses seen in x-ray tomography.

In all of the stacks collected, cell cavities in ocelli are notably more bulbous than aesthetes, which maintain a cylindrical shape that slightly tapers at the shell surface. There are no lens-less cavities of the same shape and size of the cell cavities in these samples (Figure 23D). One region appears to have a cavity of the same shape of the cell cavities, with a small lens present (Figure 23A). This region contains

a star-shaped region which is more electron dense than the epoxy but less dense than the shell. Underneath the lens is what appears to be a cluster of electron-dense material (Figure 23A,C), which others have proposed to be ACC.^[46,47] The star-shaped cluster could be a nucleation point, where microaesthetes bring ACC and nucleation-supporting impurities, initiating the formation of the lens core.

3.4 Discussion

From the growth bands, the fan-shaped microstructure, and the nucleation pit, it is clear that impurities play a crucial role in the formation of chiton ocelli lenses. The composition of these impurities is still unconfirmed. The tegmentum, or dorsal portion, of the chiton shell is known to contain many organic matrix components and etch similarly to Figure 21D, where etching does not demonstrate a preferred orientation, and no evidence of crossed lamellar structure can be observed.^[48] The shell contains 2.6% organic matrix, of which a large portion is the polysaccharide chitin, with a high concentration of glycine, so chitin and glycine-based proteins may be prevalent in the lens.^[48,49] However, β -chitin aligns with the $\langle 100 \rangle$ axis of aragonite, but the etching patterns in the lens do not match the $\langle 100 \rangle$ axis. Large concentrations of pigment are present near the lens, both in the shell and in the cell cavity,^[49] but the band color does not match the color of the pigment in the shell.

To understand the growth of the lens, it may be useful to look towards another aragonitic mollusk shell material with unique optical properties: nacre. Nacre has a layered form, with a brick-and-mortar morphology composed of pseudo-hexagonal prism aragonitic tablets sandwiched between layers of organic matrix, largely composed of chitin fibers.^[50] The fibers align with the aragonitic $\langle 100 \rangle$ axis of the tablets, providing clear, but not always consistent, orientation specification.^[31,32] The lens resembles bivalve nacre which exhibits clear $\langle 001 \rangle$ axis consistency but lacks $\langle 100 \rangle$ and $\langle 010 \rangle$ consistency^[51,52]. While the lens and nacre both employ mineral bridges to ensure crystallographic consistency, the bands in the lens do not match the periodicity of organic layers in nacre. The inconsistency in band frequency suggests not a designed hierarchy but a disordered deposition of varying amounts of aragonite precursor in the presence of impurities.

The band structure resembles that of the immature calcite sea urchin spine, which deposits layers via ACC transport through a membrane which encapsulates the spicule.^[31] A membrane could surround the lens as it grows, eventually depositing at the lens-shell interface. The membrane could regulate the transport of ACC and impurities, ensuring an impurity concentration that would support curved growth. Mineral bridges are known to ensure crystallographic continuity between nanocrystals in biominerals, allowing the crystal to encapsulate polymer and form curved surfaces and offering a pathway for ACC to crystallize into aragonite.^[53,54] Similarly, the abundance of curved and interdigitating grains may be a consequence of the ACC to aragonite transition.^[54] The electron-dense material in the rhabdom of many ocelli suggests that ACC precursors may be involved in the formation of the lens.

4 Performance of the Lens

4.1 Simulations

To investigate the impact of microstructure on optical performance of the ocelli, we conducted ray-tracing simulations using the Polaris package.^[40] The Polaris package traces rays of light in the context of crystallographic orientation. This allows us to fully account for the biaxial birefringence of aragonite. While in principle we would need to account for all grain boundaries in the cornea and lens, the sheer number, complex shape, and missing information regarding the full 3D grain structure of any given lens makes this approach intractable. We therefore chose to make the following simplifications:

1. The relevant interfaces were modeled as hemi-ellipsoids.
2. The cornea was modeled as isotropic aragonite.
3. The lens was modeled as a single crystal or 2-grain crystal of anisotropic aragonite.
4. Chromatic aberration was not considered.

4.1.1 Total internal reflection and aberrations vary between air and water

Chitons inhabit intertidal or subtidal zones. *A. granulata* live on rocks high in the intertidal zone and therefore are exposed to air for long periods of time. Speiser and coworkers predicted that the birefringence of the aragonitic lens leads to different focal lengths for rays in high (slow) and low (fast) eigenstates. They further suggested that this might allow the chiton to form an in-focus image of their environment both under water and in air.^[10] We therefore compared ray tracing figures of ocelli in air with ocelli in water (Figure 24A,B).

Due to the higher contrast in refractive indices, rays entering the cornea from air are refracted at a higher angle than rays entering from water. This results in shorter focal lengths for rays in air. The relationship between the environment change and resulting aberrations is complex. In an isotropic lens, as focal length increases, longitudinal and transverse aberrations increase. In an anisotropic lens, birefringence causes differences in aberrations between air and water.

Considering only paraxial rays, the lens in air experiences larger longitudinal aberrations than the lens in water. Because aragonite is biaxial and birefringent, deflection of light entering aragonite is not directly proportional to the refractive index of the original medium. Thus, the focal lengths of the lens in air are not directly proportional to the focal lengths in water. The extent of this effect likely varies with crystal orientation.

4.1.2 $\langle 001 \rangle$ axis orientation impacts focal length and longitudinal aberration

Rotating the $\langle 001 \rangle$ axis away from the lens optical axis increases the focal length of low rays, the impact of birefringence, and severity of longitudinal aberration. When $\alpha = 0^\circ$, the difference between the focal lengths of the high and low rays is smaller than the longitudinal aberrations apparent in either set of rays, resulting in total focal region overlap (Figure 24B-F). Observing only the mean focal length of the paraxial rays, it is apparent that α is positively correlated with focal length and degree of birefringence (Figure 24B-F). While the high focal lengths stay within a range of $0.7 \mu\text{m}$ for all α , the low focal lengths increase with α (Figure 24B-F). This increase in focal length will result in reduced transmission of signal for the low rays due to attenuation in the rhabdom^[24].

Intermediate rays can be compared to the paraxial rays to measure longitudinal aberration. As α increases, longitudinal aberration increases, contributing to a reduced depth of field (Figure 24F). However, as α and the low focal length increase, the amount of low ray signal that is focused past the edge of the cell cavity increases (Figure 24B-E). As a result, received signal in water is dominated more by the high rays, which experience less aberration, for high $\langle 001 \rangle$ axis displacement.

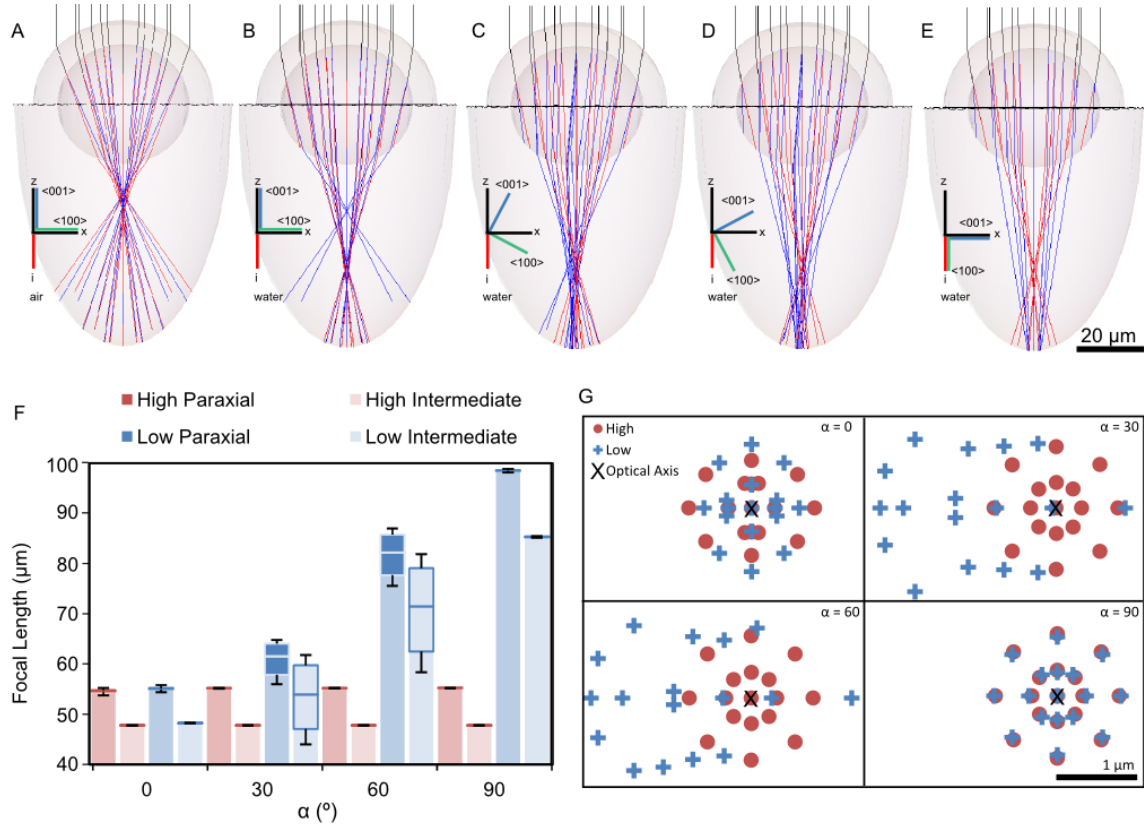


Figure 24 a-e) Ray tracing simulations in the (010) orthographic projection, showing all simulated rays. Red lines represent high rays, and blue lines represent low rays. f) Focal lengths in simulations (b-e). g) Orthographic projection of intersections between rays and the plane of least confusion for (b-e), demonstrating transverse aberration and horizontal displacement.

4.1.3 $\langle 001 \rangle$ axis orientation impacts transverse aberration

The ellipse of least confusion, which can be described as the region orthogonal to the principal ray which minimizes the mean of the squared ray displacements from the principal ray, varies based on $\langle 001 \rangle$ axis orientation. This value, which represents transverse aberration, is measured here only using rays generated at 6.7 and 13.3 μm from the principal ray in order to eliminate the impact of total internal reflection on ellipse diameter (Figure 24G).

While high ray ellipses of least confusion are small and circular, low rays can exhibit larger and more asymmetric ellipses. While the high ray transverse aberration is independent of orientation, low ray aberration depends on α . Low rays exhibit larger, less symmetric ellipses of least confusion when α is between 0° and 90° , with the diameter parallel to the rotation increasing more than the perpendicular diameter (Figure 24G).

Given a photoreceptor spacing of 7 micron, the ellipses of least confusion for rays generated less than 14 μm from the principal ray are all smaller than the photoreceptors, so these images can be resolved. However, a wider beam of incident light will produce larger transverse aberrations. Low ray ellipses exceed the critical resolution before high rays, so low rays have a smaller potential depth of field.

4.1.4 $\langle 001 \rangle$ axis orientation impacts horizontal displacement

Aggravating the large ellipse of least confusion in the low rays is the displacement of the focal point perpendicular to the principal ray. 30° and 60° rotations produce horizontal shifts in the focal point (Figure 24C,D,G). Given that the $\langle 100 \rangle$ and $\langle 010 \rangle$ axes of the grains in the lens are not aligned, the displacement can cause scattering if different rays of light travel through different grains. The horizontal displacement will contribute to uneven focus throughout images for lenses in which α is between 0° and 90° .

4.1.5 Aberrations result from crystallographic asymmetry

In isotropic lenses, lens geometry alone causes spherical aberration. In birefringent lenses, varying refraction angles are produced at different points due to lens geometry and lack of crystal rotational symmetry. The only way to counteract this effect is to align the crystal optic axis with the lens optical axis. To measure the contribution of crystal anisotropy to this aberration, we examine longitudinal aberrations within paraxial rays.

Paraxial ray aberrations depend on the orientation of the $\langle 001 \rangle$ axis (Figure 24F). High ray longitudinal aberrations decrease from 1.4 μm to 0.3 μm with increasing α . Low ray longitudinal aberrations reach up to 11 μm in medium rotations, while aberrations are smaller than 1.4 μm at 0 and 90° . Because aberrations for intermediate α values are greater than the photoreceptor spacing, lenses with $\langle 001 \rangle$ axes which are not parallel or perpendicular to the lens optical axis will experience considerable astigmatism.

4.1.6 Incident ray orientation impacts focal length and aberrations

The orientation of incoming rays influences the focal length of the lens (Figure 25A). Observing only paraxial rays at a constant α , the high ray focal length stays at 54.5 micron \pm 0.25 micron as β increases. Low ray focal length increases with β . Increasing β to 30° increases the paraxial low focal length by 5.4 micron, while increasing α to 30° increases the paraxial high focal length by 5.9 micron. The impact of rotational asymmetry is much smaller for β than for α . Increasing α to 30° results in a rotational asymmetry aberration of 8.8 μm in the low rays, while increasing β to 30° results in a rotational asymmetry aberration of 4.0 μm for low rays (Figure 25A).

Transverse aberrations are smaller for the $30^\circ \beta$ than the $30^\circ \alpha$. Astigmatism for high rays is present for β but not α . This implies that light coming from different angles will experience different focal lengths, with a small increase in rotational aberration, astigmatism and birefringence at increasing incident angles. Even if the $\langle 001 \rangle$ axis is aligned with the lens optical axis, and vertical light experiences limited birefringence, light that hits the lens at an angle will still experience birefringence.

4.1.7 Grain Boundary Orientation Impacts Transmission

Deflections across a solitary twin grain boundary range from 0° to 20° . Rays were generated at varying azimuthal and incident angles with a step size of 5° , up to 85° . Rays that do not change eigenstates experience a maximum deflection of 0.7° , which occurs at an 85° incident angle. Rays that change

eigenstates at the interface experience deflections up to 20°. Rays refracting from high to low eigenstates experience the highest deflections and earliest onset of total internal reflection.

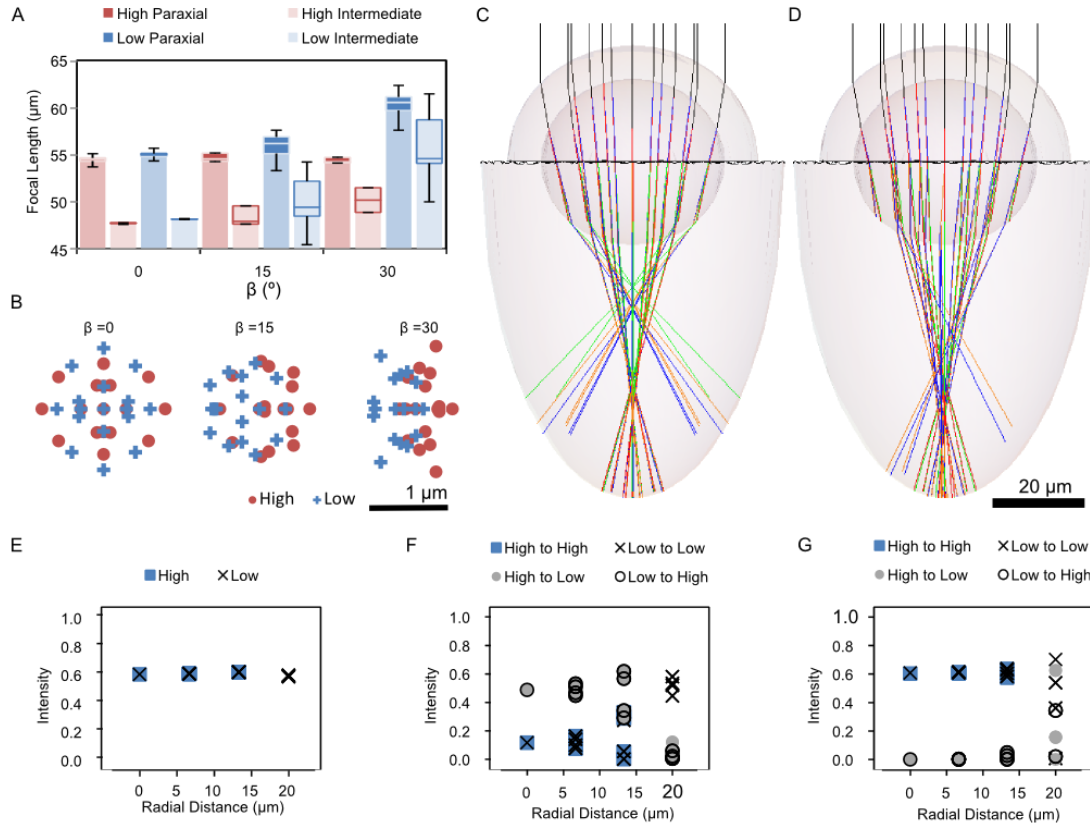


Figure 25 a) Focal lengths for lens with $\alpha=0^\circ$. b) Orthographic projection of intersections between rays and the plane of least confusion, demonstrating transverse aberration. Horizontal displacement is not to scale. c-d) Polycrystalline lenses. Red rays are high to high, orange rays are high to low, blue rays are low to low, and green rays are low to high (x to y indicates x in the top grain and y in the bottom grain). c) Lens with twin interface. d) Lens with misoriented interface. e-g) Intensities of rays transmitted through a lens with a misoriented grain boundary. e) Single crystal lens f) Lens with a twin grain boundary. g) Lens with a misoriented grain boundary.

The transmission of rays through aragonite depends on the polarization of the incoming rays, so an in situ interface was simulated. This interface was a horizontal plane incorporated into an $\alpha=0^\circ$ lens, where the top grain remains the same as in the single crystal lens, and the bottom grain is the twin of the top grain. This orientation and shape was chosen so the simulation could be compared to the single crystal control simulation, and the geometry of the interface would impact all rays equally. Real lenses exhibit a more complex microstructure, but to simulate all possible microstructures would be computationally unfeasible.

Insertion of a twin grain boundary at the center of the lens changes the paraxial focal lengths of the lens by no more than 0.16 μm , comparing sets of rays based on eigenstate in the top grain (Figure 25C). The incorporation of the twin boundary alleviates rotational symmetry-derived aberrations, decreasing the longest focal length and increasing the shortest focal length in each set of rays, reducing the longitudinal aberration from 1.37-1.42 μm to 0.56-1.14 μm .

The misoriented grain boundary induces larger changes in focal length. For high-to-low and low-to-low rays, the focal length increases by $7.76 \mu\text{m}$ compared to the $\alpha=0^\circ$ single crystal (Figure 25D). This increase in focal length more than doubles the rotational symmetry-derived longitudinal aberration for high-to-low and low-to-low rays.

Assuming that the light entering the lens is not polarized, the single crystal lens transmits all rays at $61 \pm 1\%$ of their initial intensity (Figure 25E). With the twin interface, transmission depends on the eigenstate sequence of the rays (Figure 25F). When the principal ray does not change eigenstate at the interface, it is reduced to 12% intensity. Rays that originate farther from the principal ray exhibit a diversity of transmissions. Half of the rays increase transmission with increasing distance from the principal ray, while the other half decrease transmission. Rays originating $20 \mu\text{m}$ from the principal ray exhibit up to 58% transmission, while others generated at the same distance experience total internal reflection.

Rays that change eigenstate experience higher transmissions at the center of the lens, with a principal ray transmission of 49%. Like the same-eigenstate rays, transmission increases for half of rays and decreases for the other half as the distance from the principal ray increases. Maximum transmission for the high-to-low and low-to-high rays is 62%, but four low-to-high rays and one high-to-low ray experience total internal reflection (Figure 25E).

The twin interface eliminates half of each set of rays but retains 49% transmission for a set of high rays and a set of low rays at each principal ray distance. Because the focal lengths for the single crystal lens and the twin lens are the same, the twinned lens transmits the same light as the single crystal lens, but with some rays attenuated to 49% rather than 61% and other rays attenuated to 10%. In effect, the total transmission for high rays is 61%, and the total for low rays is 61%, so the total transmission for the twin lens and the single crystal is the same.

The misoriented interface has a much more distinct difference in attenuation between eigenstates. Rays that do not change eigenstate maintain a constant $61 \pm 1\%$ transmission, regardless of the distance from the principal ray, and high-to-high rays experience total internal reflection at $20 \mu\text{m}$ while low-to-low rays are transmitted. Rays which change eigenstate are not transmitted (Figure 25F). Just like the twin lens, the misoriented lens experiences the same transmission as the single crystal lens.

Because same-eigenstate rays are transmitted through the misoriented interface, maintaining a high number of twin interfaces and low number of misoriented interfaces is important. Additional misoriented interfaces induce different focal lengths in rays that pass through different grains, scattering light and limiting the ocellus' ability to resolve images.

4.2 Transmission

Transmitting light and images through the lens allows us to directly evaluate the performance of the lens and connect the complex microstructure and composition of the lens to the optical properties of the lens. These transmission experiments demonstrate the impact of polycrystallinity on aberrations and double imaging, demonstrating what signals chitons receive.

4.2.1 Polarized light reveals crystallography

Rotating a lens between crossed polarizers reveals that different parts of the lens produce light with different polarizations. Because aragonite is birefringent, each ray of light that enters aragonite produces two rays of light with perpendicular polarizations. While the lens has the same light intensity distribution every 90° rotation, intermediate rotations highlight different parts of the lens. This can be seen in Figure 26. Two bright spots appear at the bottom left portion of the lens, reaching peaks in intensity 70° apart from each other, where images were taken in 10° increments. The two bright spots could correspond to two adjacent grains. Because the polarizations of the extraordinary rays emerging from aragonite depend on the crystallographic orientations of the grains in aragonite, the difference in brightness could come from a $\approx 70^\circ$ misorientation between the two grains. Thus, the two peaks in intensity could come from two large twinned grains, which have a misorientation of 64° .

Some animals can detect the polarization of light, including water insects and potentially some snails^[55]. Because the entire lens does not produce light with a consistent polarization, it is unlikely that chitons employ polarization filtering to limit aberrations. In a birefringent, single crystalline lens, high and low rays have different focal points (Figure 24C-E, Figure 25C-D). Without polarization detection, these focal points function as a large longitudinal aberration. If the lens is a single crystal and the animal has the sensory capabilities to detect the polarization of light, then it could detect high and low rays separately, receiving an image with fewer aberrations than the aggregate image. However, ocelli lenses are polycrystalline, and the disparate $\langle 100 \rangle$ and $\langle 010 \rangle$ axes across the lens produce light with different polarizations in different parts of the lens, so polarization detection would result in the reception of partial images.

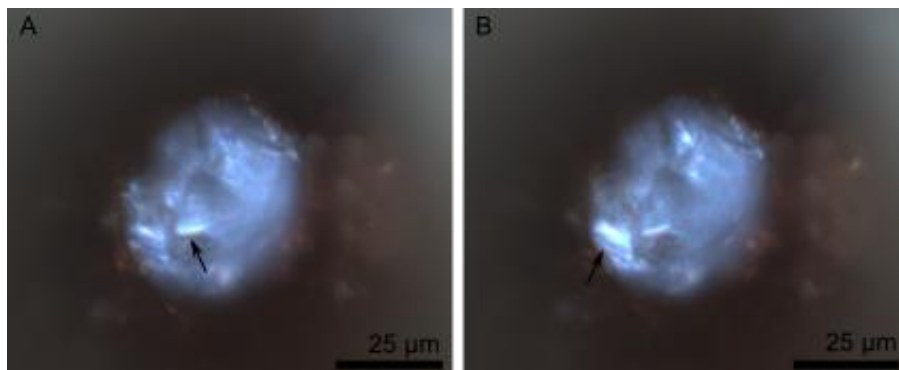


Figure 26. A) Ocellus in shell, between crossed polarizers. B) Ocellus in A, rotated counterclockwise by 70° .

4.2.2 The lens transmits images

“N” masks transmitted through lenses demonstrate the variety of performance from lens to lens. Images transmitted through lenses are distorted, but the nature of the distortions varies between lenses. While some lenses transmit the shape of the mask accurately (Figure 27E), other lenses distort the shape. In

Figure 27B, the lens transmits a clear, intense “N”, but the image is elongated vertically, and several fainter images are projected beside the primary image. This “ghosting” effect can be seen in most lenses after moving the mask and refocusing (Figure 27C, F).

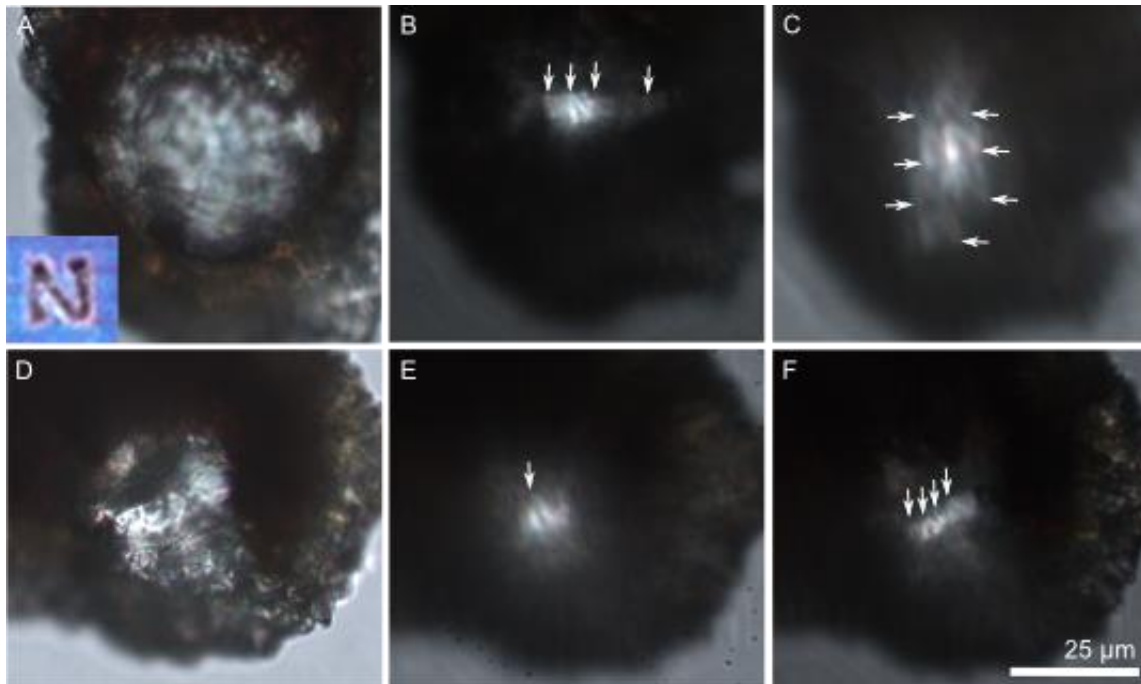


Figure 27. N mask transmitted through ocelli. White arrows indicate projected “N” images. A,D) Ocellus without mask. Mask is shown in A (inset). B,E) Ocellus with N in focus. C,F) Ocellus with N out of focus.

In an amorphous calcium carbonate (ACC) lens, some ghost images can be observed in a non-confocal microscope. Unlike the ghost images seen in the aragonite lenses, the ghost images in the amorphous calcium carbonate lens are not horizontally displaced and are merely enlarged, unfocused versions of the focused image (Figure 28B).

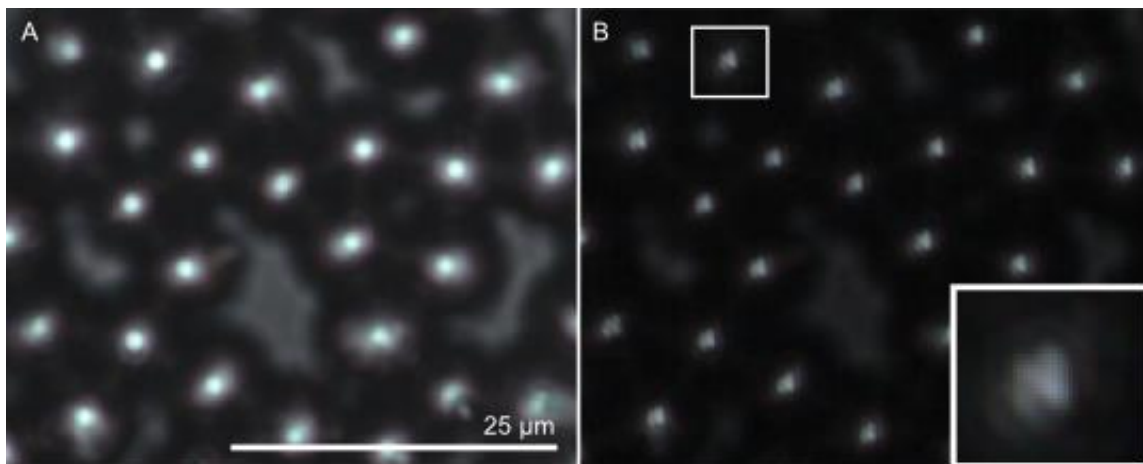


Figure 28. N mask transmitted through amorphous calcium carbonate microlens array. A) Array without mask. B) Array with mask.

Unlike the ghost images seen through ACC lenses, the ghost images in the ocelli lenses have unreliable number, size, shape, location, and intensity. As many as seven distinct images have been observed through ocelli lenses (Figure 27C). In a single crystal aragonite lens, horizontally displaced double images can appear when the focal point of the low rays is displaced horizontally at α values between 0° and 90° (Figure 24C-D). In this case, one image can be focused at a time. However, no more than two images should be transmitted for a single crystalline lens. In a polycrystalline lens, any set of low rays which have entered a grain at an α value between 0° and 90° can have a horizontally displaced focal point (Figure 25D). More grains in the lens produce more displaced images. Thus, the multitude of images is likely a result of the polycrystallinity of the lens. Whether these double images are purely produced by non-twin grain boundaries as predicted in Figure 25C-D is unknown.

4.2.3 Laser ray tracing demonstrates aberrations in the lens

Laser light was traced through extracted ocelli which were flanked by attached pigmented shell. When passed through lenses, laser light is split into smaller rays, potentially due to interference from path length differences between rays which take different trajectories through the lens. The experiments resulted in three-dimensional image stacks containing up to 290 million pixels and thousands of rays. In order to measure aberrations in the ray trace, one could measure the brightest region in the ray trace, which would represent the focal region. However, unlike ray traces from amorphous lenses or crystalline lenses with simpler microstructure^[16,23,56], chiton ocelli lenses produce focal regions with complex shape that is not clearly defined (Figure 30B,C,E,F). Additionally, some light is refracted through the fractured shell adjacent to the lens into the light path in this setup. In vitro, the pigment surrounding the rhabdom would eliminate bleed-through. Therefore, this study uses ray tracing to detect and eliminate rays coming from the shell and to detect ray intersections which would allow us to measure aberrations.

4.2.3.1 Longitudinal aberration

Due to the multitude of rays, three-dimensional line detection for calculation of intersections is intractable. The three-dimensional random Hough transform described by Qiu^[57-59] produced only 19422 transformed pixels in 500 seconds using MATLAB, and fewer than a quarter of the points contributed to lines with at least a two-segment consensus. Furthermore, the four-dimensional array required to transform three-dimensional lines has a memory-limited step size which would make ray detection inaccurate. The quick three-dimensional random Hough transform described by Qiu made this problem less computationally intensive by only using edges, by only detecting one line, and by using a compressed image. However, the ray tracing stacks in this experiment cannot be compressed because compression will remove fine delineations between lines which we are trying to detect, and Canny edge detection and non-maxima suppression both result in grainy, non-continuous lines for these images.

Because accurate three-dimensional line detection algorithms demonstrated excessive time and space complexity for this application, we instead use double two-dimensional line detection. Using a standard two-dimensional Hough transform, weighting points by intensity, we can transform over 8 million points in 29 seconds using MATLAB with an angle sensitivity of 0.25° and a radius sensitivity of 0.25 px. After running the two-dimensional Hough transform on projections along the width and height of the stack and collecting line intersections, we can compare detected intersections and remove false intersections from skew lines. The highest and lowest intersections define the longitudinal aberration of the trace.

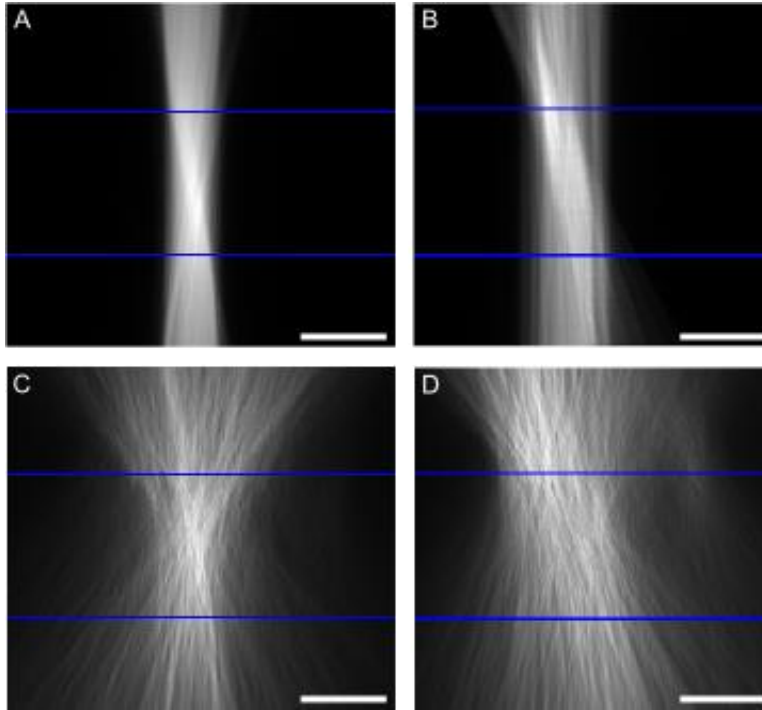


Figure 29. Recalculated ray traces. Blue lines indicate top and bottom of focal region A,B) Ray traces of C,D created by detecting lines in stack projections. Lines that start within 20 μm of the centroid of the non-zero points in the top row are plotted. C,D) Projections of a ray trace perpendicular to the ray direction. Scale bars 25 μm .

The average longitudinal aberration is $65.7 \pm 17.0 \mu\text{m}$, which is considerably longer than the 1 - 13 μm aberrations calculated in the simulations. In fact, the longitudinal aberration would fill the entire cell cavity. However, the calculated longitudinal aberration is subject to several calculation parameters that impact the definitions of intersections.

As the first parameter, in order to be considered for intersections, line origins must correspond to points of certain intensity on the original image. The critical intensity here is defined as 50% of the maximum intensity of the first row of the image; however, a different threshold would change the rays which are considered when finding intersections.

The most important parameter is the critical angle between rays that defines if an intersection is included. Consider the paraxial rays, which lie next to the principal ray and have the longest intersection distance, thus having a strong impact on the focal length of the lens. The focal length determined by the paraxial rays approaches infinity as the initial distance between the paraxial rays and the principal ray approaches 0. In effect, all lenses have a focal length of infinity at the center of the lens, as the curvature of an infinitesimally small segment of the center of the lens is 0. Thus, in order to measure a tangible focal length, it is necessary to define a critical angle between rays that filters out rays that are nearly parallel. In this experiment, the critical angle is defined as the maximum angle between rays in the sample divided by 1.3. A larger critical angle would result in smaller calculated longitudinal aberrations, and a smaller critical angle would result in larger aberrations.

Additionally, several parameters are incorporated into the ray detection program. The resolution of the Hough transform matrix, which determines the precision to which the program measures angles and radii,

is set to 0.25° and 0.25 px. However, a finer mesh may produce a finer, more accurate set of rays, and a looser mesh could produce a set of more intense, distinct rays. The stopping conditions could also alter the ray output to consider only the most intense rays or to consider a greater diversity of rays.

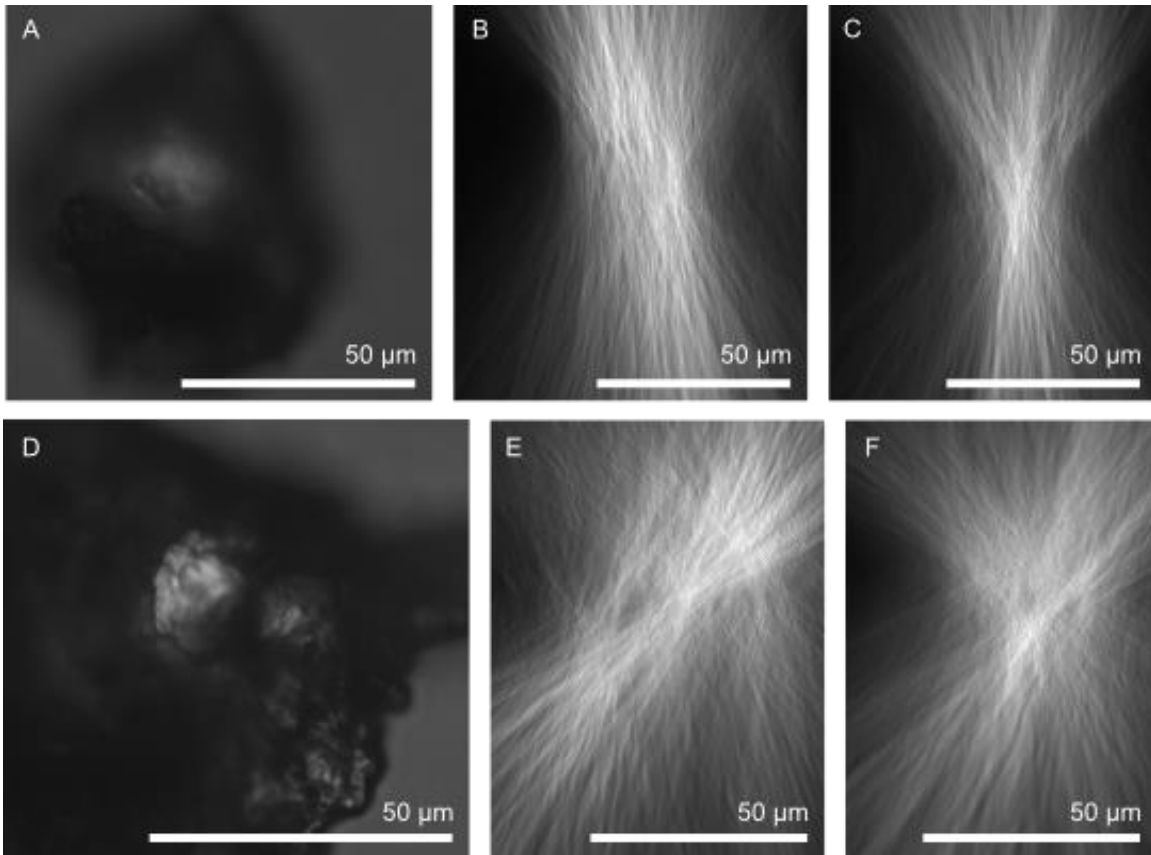


Figure 30. Projections of laser path transmitted through ocellus. A, D) Polarized light micrograph of ocelli. B,C) Projections of A ray trace along height(B) and width(C). E,F) Projections of D ray trace along height(E) and width(F).

Despite the intricacies of retracing rays after image capture, it is indisputable that the ray traces exhibit larger aberrations than those calculated in simulations (Figure 29). No traces exhibit multiple distinct focal points. While some traces demonstrate multiple distinct points of high intensity (Figure 30E), these points share some rays, and it is difficult to define where one focal point begins and the other ends. The multiple focal points reflect the multiple images found in Figure 27. The multiple ray convergence points in the ray traces translate into multiple images which vary in clarity and coherence at different focal lengths. The multiple focal points arise because of the birefringence of aragonite, and the blurred focal points come from low angle grain boundaries, defects, non- $\langle 001 \rangle$ misorientation axis grain boundaries, and possibly impurities. These mechanisms produce an array of focal points that translates into a single image with a large longitudinal aberration. Because the signal is muddled, it is unlikely that the chiton can filter between focal points using its nervous system. While it is possible that a lens with a misaligned $\langle 001 \rangle$ axis can have a low focal point beyond the boundary of the rhabdom while underwater, such that only the high ray focal point is in the rhabdom, the remaining signal will still have large aberrations.

4.2.3.2 Transverse aberration

By iterating through z-values and measuring the root mean square distance between points and their centroid, we can determine the transverse aberration of the ray trace. Here, we use projections rather than three-dimensional stacks for consistency.

The measured transverse aberration for unmodified projections is $29.4 \pm 10.4 \mu\text{m}$. This is considerably larger than the calculated 1-3 μm transverse aberrations. The discrepancy comes largely from light that bleeds through the nearby shell and refracts into the ray trace, increasing the diameter of the light path. With recalculated images that only include rays within a 40 μm diameter, the measured transverse aberration decreases significantly to $6.5 \pm 2.0 \mu\text{m}$, on the same order of the simulated values and near the 7 μm sensory cell size. Still, the measured transverse aberration is higher than the simulation values. The discrepancy is a consequence of the increased number of grain boundaries, small angle grain boundaries that distort the orientation of the $\langle 001 \rangle$ axis, and inconsistent refractive indices due to varying impurity concentrations in the bands, all of which were not taken into account in the simulations. The large transverse aberration implies that the resolution of ocelli is not always limited by the size of the sensory cells. Instead, many lenses contain aberrations that are greater than the size of the sensory cells, such that the lens quality is the limiting factor in the resolution of the ocellus.

4.3 Discussion

By considering the birefringence of the lens in the simulations, this study explains not only the importance of microstructure, $\langle 001 \rangle$ alignment, and $\langle 001 \rangle$ orientation, on the optical properties of the lens; it also explains basic behaviors of birefringent lenses. Because the $\langle 001 \rangle$ axis of the lens is not controlled, much like the slightly asymmetric shape of the lens and cell cavity, the lens is predisposed to birefringence and horizontal focal point deviation. Though the lens does not have a large imaging radius, the overall performance of the lens is hindered by the fact that incident rays of light that enter at an angle greater than 0° experience different focal lengths and aberrations than the rays of light entering parallel to the lens optical axis. This principal is reflected in other biomineral lenses. In trilobites, the birefringent lenses are incorporated into a compound eye, with the calcite $\langle 001 \rangle$ axis (which is equal to the calcite optic axis) parallel to the length of the rhabdom, such that only light that enters parallel to the lens optical axis is collected. Likewise, in brittlestar lenses, the calcite $\langle 001 \rangle$ axis is parallel to the lens optical axis, allowing the lens to focus all light to a single focal point, which corresponds to a sensory cell bundle. However, the ocellus lens must transmit light from multiple directions in order to facilitate spatial imaging, so these birefringence limiting techniques would not apply to the chiton.

Previous studies have demonstrated that chitons with ocelli respond to light signals, albeit more slowly than lens-less chitons, and they respond to spatial targets more readily than the lens-less chitons.^[10,24] From transmission of images, it is clear that the lens is capable of producing images, although the images are distorted, don't have a consistent focal point, and contain many doubled images. It is possible that the chiton can adjust to the double images by combining the signals from its hundreds of ocelli. Alternatively, because the double images likely come from a combination of misoriented grains and birefringence, the chiton could separate the double images if it has the sensory capabilities for polarization detection.

5 Conclusions

From analysis of formation paths and impurities, microstructure, lens optics, and optical performance, this study has explored processing-structure-properties-performance relationships in chiton ocelli lenses.

Electron backscatter diffraction (EBSD) reveals that unlike brittlestar lenses, these lenses are polycrystalline. Like trilobite lenses, the orientation of the $\langle 001 \rangle$ axis in the lens is controlled. Unlike the trilobite lenses, ocelli lenses have a $\langle 001 \rangle$ axis that exhibits small deviations within each grain and across grains, but rather than fanning out from a central point, the $\langle 001 \rangle$ axis deviations are random. While the $\langle 001 \rangle$ axis is finely aligned, it is still less aligned than a geological single crystal, indicating that the lens will not behave like a single crystal.

EBSD maps also indicate that the grains take on a fan-shaped morphology. This pattern is supported by etching structure, which indicates growth bands running perpendicular to the growth of the fan-shaped grains. Furthermore, a pore at the lens-shell interface at the source of the growth bands indicates that a packet of impurities and amorphous calcium carbonate (ACC) may support the rapid nucleation of the lens. Though in many biomineral systems, a single nucleation point indicates that the mineral will be a single crystal, these lenses are polycrystalline and highly twinned. The core of the growth bands has a complex, anisotropic structure, indicating that small twinned grains may form the nucleus of the crystal, and large grains which are consequently twinned grow from the seed. Because the twinning originates in the center of the lens, the twin interfaces between the larger grains are not flat and parallel to the (110), as coherent twins would be. Thus, the interfaces become incoherent twins.

Transmission experiments, explained by simulations, demonstrate the impact of polycrystallinity and orientation on the performance of the lens. Large aberrations are present in ray traces, which may originate from misalignment of the incident beam with the lens optical axis, misalignment of the incident beam with the $\langle 001 \rangle$ axis, and aberrations resulting from the many grains present in the lens. Though a single crystalline lens with an optic axis deviating from the lens optical axis would exhibit two distinct focal points, few lenses show two distinct focal points and instead spread signal across a large longitudinal and transverse area. This results from a combination of the birefringence and polycrystallinity of the lens, as well as surface roughness on the lens. Most importantly, every ray trace and image transmission tested in this experiment demonstrated a different ray trace shape, aberration size, and image intensity and clarity, reflecting the diversity seen in etching and EBSD.

From these experiments, we can take steps towards improving the formation of synthetic calcium carbonate lenses and learn about the image formation capabilities of the chiton. That chitons have spatial vision at all is remarkable, considering the large aberrations present and the polycrystallinity of the lens, but the chiton may be able to overcome the shortcomings of the lens because of the continuous rhabdom filling the entire cell cavity. However, a significant amount of processing power would be necessary for an animal to understand the multiple images and high aberration. Whether chitons have the necessary processing power remains to be seen.

6 References

- [1] A. Finomore, P. Cunha, T. Shean, S. Vignolini, S. Guldin, M. Oyen, U. Steiner, *Nat Commun* **2012**, *3*, 966.
- [2] H. D. Espinosa, J. E. Rim, F. Barthelat, M. J. Buehler, *Prog. Mater. Sci.* **2009**, *54*, 1059.
- [3] G. M. Luz, J. F. Mano, *Philos. Trans. R. Soc. Math. Phys. Eng. Sci.* **2009**, *367*, 1587.
- [4] P. Qiu, C. Mao, *ACS Nano* **2010**, *4*, 1573.
- [5] Y. N. Kul'chin, S. N. Bagaev, O. A. Bukin, Voznesenskiĭ, *Tech. Phys. Lett.* **2008**, *34*, 633.
- [6] C. Jansson, T. Northen, *Curr. Opin. Biotechnol.* **2010**, *21*, 365.
- [7] J. Blamey, E. J. Anthony, J. Wang, P. S. Fennell, *Prog. Energy Combust. Sci.* **2010**, *36*, 260.
- [8] H. E. Dunsmore, *Energy Convers Mgmt* **1992**, *33*, 565.
- [9] L. M. Gordon, D. Joester, *Nature* **2011**, *469*, 194.
- [10] D. I. Speiser, D. J. Eernisse, S. Johnsen, *Curr. Biol.* **2011**, *21*, 665.
- [11] M. R. Lee, C. Torney, A. W. Owen, *Palaeontology* **2007**, *50*, 1031.
- [12] M. R. Lee, C. Torney, A. W. Owen, *Chem. Geol.* **2012**, *314-317*, 33.
- [13] C. Torney, Mineral eyes: lessons from the natural world, University of Glasgow, 2011.
- [14] C. Torney, M. R. Lee, A. W. Owen, *Palaeontology* **2013**.
- [15] C. Torney, M. R. Lee, A. W. Owen, *Appl. Texture Anal. Ceram. Trans.* **2009**, *201*, 619.
- [16] E. Clarkson, R. Levi-Setti, *Nature* **1975**, *254*, 663.
- [17] C. Torney, M. R. Lee, A. W. Owen, *Adv. Trilobite Res. Cuad. Mus. Geomin.* **2008**, *9*, 389.
- [18] J. Miller, E. N. K. Clarkson, *Philos. Trans. R. Soc. Lond.* **1980**, *288*, 461.
- [19] J. Aizenberg, A. Tkachenko, S. Weiner, L. Addadi, G. Hendler, *Nature* **2001**, *412*, 819.
- [20] J. Aizenberg, G. Hendler, *J. Mater. Chem.* **2004**, *14*, 2066.
- [21] I. Schmidt, K. Lee, E. Zolotoyabko, P. Werner, T. S. Shim, Y.-K. Oh, P. Fratzl, W. Wagermaier, *ACS Nano* **2014**, 9233.
- [22] W. Wagermaier, I. Schmidt, P. Fratzl, **2010**.
- [23] K. Lee, W. Wagermaier, A. Masic, K. P. Komareddy, M. Bennet, I. Manjubala, S.-W. Lee, S. B. Park, H. Cölfen, P. Fratzl, *Nat. Commun.* **2012**, *3*, 725.
- [24] P. R. Boyle, *Nature* **1969**, *222*, 895.
- [25] L. R. Brooker, Revision of Acanthopleura Guilding, 1829 (Mollusca: Polyplacophora) based on light and electron microscopy. Doctor of Philosophy, Murdoch University: Western Australia, 2003.
- [26] W. L. Bragg, *Proc. R. Soc. Math. Phys. Eng. Sci.* **1924**, *105*, 370.
- [27] H. A. Lowenstam, *Science* **1981**, *211*, 1126.
- [28] F. C. Meldrum, S. T. Hyde, *J. Cryst. Growth* **2001**, *231*, 544.
- [29] S. Albeck, J. Aizenberg, L. Addadi, S. Weiner, *J. Am. Chem. Soc.* **1993**, *115*, 11691.
- [30] A. Berman, L. Addadi, A. Kvick, L. Leiserowitz, M. Nelson, S. Weiner, *Science* **1990**, *250*, 664.
- [31] S. Weiner, L. Addadi, *J Mater Chem* **1997**, *7*, 689.
- [32] F. Nudelman, B. A. Gotliv, L. Addadi, S. Weiner, *J. Struct. Biol.* **2006**, *153*, 176.
- [33] J. Aizenberg, *Science* **2003**, *299*, 1205.
- [34] M. I. Aroyo, J. M. Perez-Mato, D. Orobengoa, E. Tasci, G. de la Flor, A. Kirov, *Bulg Chem Commun* **2011**, *43*, 183.
- [35] M. I. Aroyo, J. M. Perez-Mato, C. Capillas, E. Kroumova, S. Ivantchev, G. Madariaga, A. Kirov, H. Wondratschek, *Z Krist* **2006**, *221*, 15.
- [36] M. I. Aroyo, A. Kirov, C. Capillas, J. M. Perez-Mato, H. Wondratschek, *Acta Cryst* **2006**, *A62*, 115.
- [37] F. J. Humphreys, *J. Mater. Sci.* **2001**, *36*, 3833.
- [38] F. J. Humphreys, *Scr. Mater.* **2004**, *51*, 771.
- [39] P. Leong, S. Carlile, *J. Neurosci. Methods* **1998**, *80*, 191.
- [40] W. S. T. Lam, S. McClain, G. Smith, R. A. Chipman, In *Polarization in Optical Design (IWA)*; Optical Society of America: Jackson Hole, Wyoming, United States, 2010.
- [41] P. V. C. Hough, Method and means for recognizing complex patterns **1962**.

- [42] N. V. Wilmot, D. J. Barber, J. D. Taylor, A. L. Graham, *Philos. Trans. Biol. Sci.* **1992**, 21.
- [43] B. Jones, R. W. Renaut, *Sedimentology* **1996**, 43, 323.
- [44] R. W. Renaut, B. Jones, *Can. J. Earth Sci.* **1997**, 34, 801.
- [45] P. U. P. A. Gilbert, F. H. Wilt, In *Molecular Biomineralization*; Müller, W. E. G., Ed.; Springer Berlin Heidelberg: Berlin, Heidelberg, 2011; Vol. 52, pp. 199–223.
- [46] M. J. Connors, Design of a Multifunctional Biomineralized Armor System: The Shell of Chitons, Massachusetts Institute of Technology, 2014.
- [47] L. Li, Biomineralized Structural Materials with Functional Optical Properties, Massachusetts Institute of Technology, 2014.
- [48] M. J. Connors, H. Ehrlich, M. Hog, C. Godeffroy, S. Araya, I. Kallai, D. Gazit, M. Boyce, C. Ortiz, *J. Struct. Biol.* **2012**, 177, 314.
- [49] W. Haas, K. Kriesten, *Zoomorphologie* **1978**, 90, 253.
- [50] Y. Levi-Kalisman, *J. Struct. Biol.* **2001**, 135, 8.
- [51] A. G. Checa, J. H. Cartwright, M.-G. Willinger, *Proc. Natl. Acad. Sci.* **2009**, 106, 38.
- [52] A. G. Checa, H. Mutvei, A. J. Osuna-Mascaró, J. T. Bonarski, M. Faryna, K. Berent, C. M. Pina, M. Rousseau, E. Macías-Sánchez, *J. Struct. Biol.* **2013**, 183, 368.
- [53] Y. Oaki, A. Kotachi, T. Miura, H. Imai, *Adv. Funct. Mater.* **2006**, 16, 1633.
- [54] A. J. Goetz, D. R. Steinmetz, E. Griesshaber, S. Zaefferer, D. Raabe, K. Kelm, S. Irsen, A. Sehrbrock, W. W. Schmahl, *Acta Biomater.* **2011**, 7, 2237.
- [55] G. Horváth, D. Varju, *Polarized Light in Animal Vision*; 1st ed.; Springer, 2010.
- [56] E. Gu, H. W. Choi, C. Liu, C. Griffin, J. M. Girkin, I. M. Watson, M. D. Dawson, G. McConnell, A. M. Gurney, *Appl. Phys. Lett.* **2004**, 84, 2754.
- [57] W. Qiu, M. Ding, M. Yuchi, IEEE, 2008; pp. 449–452.
- [58] A. Miraliakbari, M. Hahn, H. Arefi, J. Engels, *Int. Arch. Photogramm. Remote Sens. Spat. Inf. Sci. ISPRS Beijing China* **2008**, 1417.
- [59] T. Schenk, *ISPRS J. Photogramm. Remote Sens.* **2004**, 58, 315.

7 Acknowledgments

I owe many thanks to my advisor, Dr. Derk Joester, for supporting my ideas and advising me through this work. I am also grateful for the Joester group – Dr. Lyle Gordon, Mike Cohen, Mike Whittaker, Emmie Campbell, Karen Derocher, and Robert Free – for helping me with many aspects of this work. I also owe many thanks to Dr. Kathleen Stair for all of her help as senior thesis advisor.

Several collaborators helped me with this work. The Chipman Group at the University of Arizona – Dr. Russell Chipman and Tiffany Lam – was indispensable for the simulations. Their expertise and programming support were critical for helping me understand the relationship between crystallography of the lens and its performance. The Perez-Huerta group at the University of Alabama was very helpful, not only providing samples but also sharing their findings with EBSD and etching. I owe many thanks to Dr. Stuart Stock from the Feinberg School of Medicine for collecting x-ray tomography scans and helping me understand the data. I also owe thanks to Tyler Rehak from the Northwestern physics department for lending me equipment for the transmission experiments.

This work was supported by two funding sources. It was assisted by a grant from the Undergraduate Research Grant Program which is administered by Northwestern University's Office of the Provost. However, the conclusions, opinions, and other statements in this publication are mine and not necessarily those of the sponsoring institution. This research was also sponsored by the Chemistry of Life Processes CAURS Fellowship.

This work made use of the EPIC facility (NUANCE Center-Northwestern University), which has received support from the MRSEC program (NSF DMR-1121262) at the Materials Research Center, The Nanoscale Science and Engineering Center (EEC-0118025/003), both programs of the National Science Foundation; the State of Illinois; and Northwestern University. It also made use of the OMM Facility supported by the MRSEC program of the National Science Foundation (DMR-1121262) at the Materials Research Center of Northwestern University.